# STUDY OF ELECTRON IDENTIFICATION IN THE OPERA DETECTOR

A THESIS SUBMITTED TO
THE GRADUATE SCHOOL OF NATURAL AND APPLIED SCIENCES
OF
MIDDLE EAST TECHNICAL UNIVERSITY

BY

M.FATİH BAY

IN PARTIAL FULFILLMENT OF THE REQUIREMENTS
FOR
THE DEGREE OF MASTER OF SCIENCE
IN
PHYSICS

JULY 2008

Approval of the Graduate School of Natural and Applied Sciences.

Prof. Dr. Canan Özgen
Director

I certify that this thesis satisfies all the requirements as a thesis for the degree of Master of Science.

Prof. Dr. Sinan Bilikmen
Head of Department

This is to certify that we have read this thesis and that in our opinion it is fully adequate, in scope and quality, as a thesis for the degree of Master of Science.

Assoc. Prof. Dr. Ali Murat Güler
Supervisor

Examining Committee Members

Prof. Dr. Ali Ulvi Yılmazer (Ankara Uni.,PHYS) _____

Assoc. Prof. Dr. Ali Murat GÜLER (METU,PHYS) _____

Prof. Dr. Mustafa Savcı (METU,PHYS) _____

Prof. Dr. Gürsevil Turan (METU,PHYS) _____

Assist. Prof. Sadi Turgut (METU,PHYS) _____

"I hereby declare that all information in this document has been obtained and presented in accordance with academic rules and ethical conduct. I also declare that, as required by these rules and conduct, I have fully cited and referenced all material and results that are not original to this work."

Name Surname : M.FATİH BAY

Signature :

ABSTRACT

STUDY OF ELECTRON IDENTIFICATION IN THE OPERA DETECTOR

M.FATİH, BAY

M.S., Department of Physics

Supervisor: Assoc. Prof. Dr. Ali Murat Güler

July 2008, 78 pages.

The OPERA experiment is designed to perform first direct observation of $\nu_\tau$ appearance in an almost pure $\nu_\mu$ beam. The OPERA detector is a hybrid set-up which combines a lead/emulsion target with various electronic detectors. It is located in Gran Sasso Laboratory (LNGS), 730 km away from CERN where neutrino beam is produced. A good electron identification in the ECC brick would also allow OPERA to search for $\nu_\mu \rightarrow \nu_e$ oscillations. We have studied electron identification in the Emulsion Cloud Chamber (ECC) brick which was exposed to CERN SPS H4 electron beam. Emulsion scanning was performed in LNGS scanning laboratory. FEDRA framework was used for the data analysis. In total, we have found 30 electron showers in the brick. The characteristics of

each shower have been studied. The background base-track contamination in the shower was estimated as $20 \pm 4$. This is mainly due to shower overlap of electrons and passing through cosmic rays.

Keywords: Neutrino, Neutrino Oscillations, ECC, Electron identification.

# ÖZ

## OPERA DEDEKTÖRÜNDE ELEKTRONUN TANIMLANMASI

M.FATİH, BAY
Yüksek Lisans , Fizik Bölümü
Tez Yöneticisi: Doç. Dr. Ali Murat Güler

Temmuz 2008, 78 sayfa.

OPERA deneyi yüksek oranda saf müon nötrino demeti içersinde $\nu_\tau$'nun ilk direk gözlenmesi amacıyla dizayn edilmiş bir deneydir. OPERA dedektörü bir kurşun/emülsiyon hedef (ECC) ile çeşitli elektronik dedektörlerinin kombinasyonu sonucu oluşturulmuş hibrit bir sistemdir. Dedektör, nötrino demetinin üretildiği CERN'den 730 km uzaklıkta, Gran Sasso Laboratuvarında (LNGS) konumlanmıştır. ECC dedektörü içerisindeki iyi elektron tanımlanma özelliği, OPERA'ya müon nötrinosundan elektron nötrinosuna salınımları için araştırma yapma imkanıda tanımaktadır. CERN SPS H4 elektron demetine maruz bırakılmış ECC dedektörü içerisinde elektron tanımlama işlemini araştırdık. Emülsiyon tarama işlemi LNGS mikroskop laboratuvarında yapıldı. Veriler FEDRA iskeleti

aracılığıyla analiz edildi. Toplamda, ECC dedektör içersinde 30 elektron duşu bulundu. Her bir duşun karakteristiği araştırıldı. Duş içersindeki arkaplan $20 \pm 4$ olarak bulundu. Bunlar duşların üst üste binmesinden ve kozmik ışınlardan kaynaklanmıştır.

Anahtar Kelimeler: Nötrino, Nötrino Salınımları, ECC Dedektör, Elektron Duş.

to my parents and sisters

# ACKNOWLEDGMENTS

The work presented in this thesis would not have been possible without the involvement of a number of people. I would especially like to thank the following persons in particular:

I would like to express my gratitude to my supervisor Assoc.Prof. Dr. Ali Murat GÜLER for his close cooperation through out my thesis and also for his guidance in teaching me all that I have learned in the field of data analysis by giving me the opportunity to work as a member at the METU HEP group.

My sincere thanks go to Volkan ÇUHA for leading me through out this work with great patience. I owe special thanks to Serhan TUFANLI from whom I have had invaluable help on data analysis.

I am deeply indebted to LNGS laboratory where I spent six months, to INFN for providing me financial support through FAI fund, to LNGS scanning group for helping me in scanning emulsion plates, to CS facility team for working with me at CS Facility and finally to CERN test exposure team for their contributions. I also thank my colleague Kadir OCALAN and all the friends I have met in these three years at METU.

# TABLE OF CONTENTS

# LIST OF FIGURES

# LIST OF TABLES

# CHAPTER 1

# INTRODUCTION

Neutrino physics has always been, and is still an attractive topic for a long time in the high energy physics. The Standard Model (SM) of particle physics assumes that neutrinos are massless fermions. Therefore, physics of massive neutrino is beyond the Standard Model. The clearest signature of massive neutrino is the observation of neutrino oscillations which was first predicted by Pontecorvo [1] in 1957. The evidence of neutrino oscillation was first found in the Super-Kamiokande experiment in 1998 [2, 3]. This observation has been confirmed in Solar neutrino experiments and in the long baseline accelerator experiments.

Although there are several experimental results for neutrino oscillations, a direct search for $\nu_\tau$ appearance is still missing. Oscillation Project with Emulsion-tRacking Apparatus (OPERA) experiment [4] is designed to search for the $\nu_\tau$ appearance in an almost pure $\nu_\mu$ beam produced at CERN SPS to LNSG. The signature of $\nu_\tau$ appearance will be the observation of $\nu_\tau$ charged current(CC) interactions and subsequent decay of $\tau$-lepton in the ECC brick of the OPERA detector.

This thesis deals with electron identification in the OPERA detector. It is based on shower development in the ECC brick which was exposed to CERN SPS H4-beam line. Emulsion plates were developed and scanned in LNGS underground laboratory in Italy. The Framework for Emulsion Data Reconstruction

and Analysis (FEDRA) was used for the data analysis.

The thesis's organization can be classified as follows:

- The second Chapter includes a general description of the neutrinos, its oscillation phenomenology and a review of experiments related to atmospheric, solar, reactor and long-baseline accelerator neutrino experiments.

- In the third Chapter a detailed description of the OPERA detector will be given.

- Emulsion scanning system used for scanning will be explained in the fourth Chapter.

- In the fifth Chapter, the test beam exposure at CERN SPS H4-beam line, and emulsion scanning of the ECC brick will be mentioned.

- In the sixth Chapter, data analysis for electron shower reconstruction will be presented.

- The last chapter includes the conclusion.

# CHAPTER 2

# PHENOMENOLOGY OF NEUTRINO OSCILLATIONS

## 2.1 Historical Background

Experiments by Meitner and Hahn as well as Chadwick [5] had shown that the beta-decay process had a continuous energy spectra rather than the discrete spectra predicted by a two-body decay. In addition, the Rutherford model [6] was unable to properly describe the total spin of nuclei and it had even been suggested that energy and spin were only conserved on a statistical level. Neutrino physics was then born on December 4, 1930, as Pauli proposed the existence of the "neutron", a new spin 1/2 particle with small mass and no electric charge, in a letter to a physicist meeting in Tubingen. As Pauli himself stated in the letter, this was a "desperate remedy" in order to save the conservation of energy and angular momentum as only two elementary particles, the proton and the electron, were believed to exist at this time. The fact that the "neutron" had not yet been discovered was implied by its weak interaction with matter due to the lack of electric charge. Two years later, in 1932, Chadwick made the experimental discovery of the neutron [7]. However, it was clear that this particle could not be the same as Pauli's "neutron", since it was too heavy. Thus, Fermi renamed Pauli's neutron to "neutrino", meaning neutral and small, in 1933.

In 1956, after a four-year search, F. Reines and C. L. Cowan finally succeeded in detecting neutrinos produced by the Savannah River Reactor in South Carolina [8]. In this laboratory, they constructed a large tank of water. In the tank, they detected the distinct signature of the nuclear interaction: $\overline{\nu_e} + p \rightarrow n + e^+$ which is initiated by the electron anti-neutrino. With the invention of new accelerators and sophisticated detectors, it is now known that each neutrino comes with its own family of quarks and leptons [9]. By 1962, a particle accelerator at Brookhaven National Laboratory was generating enough neutrinos to conduct detection experiments. The existence of a second type of neutrino, the muon neutrino $\nu_\mu$, was confirmed by the Brookhaven National Laboratory in 1962 [10]. When the third charged lepton, the tau $\tau^-$, was discovered in 1975 [11], it was natural to assume that it would also have a neutrino associated to $\tau$-lepton. However, it was not until 2000 that the tau neutrino ($\nu_\tau$) was actually detected by the DONUT collaboration [12], completing the third generation of fermions in the Standard Model of particle physics.

## 2.2 Massless Neutrinos in the Standard Model

Local (gauge) symmetries and the connection between forces mediated by spin-1 particles have been the greatest success of the modern particle physics. In the Standard Model, formulated by Glashow [13], Weinberg [14] and Salam [15], the gauge groups, which are SU(3), SU(2) and U(1) respectively, connect the strong, weak and electromagnetic interactions to each other. The properties of the interactions are defined by the related symmetry group in which they are. The SM of particle physics is a theory that describes three of the four known fundamental interactions between the elementary particles that make up all matter [16]. This theory unifies the electroweak theory and quantum chromodynamics into a

structure denoted by the gauge groups

$$G_{SM} = SU(3)_c \times SU(2)_L \times U(1)_Y, \tag{2.1}$$

with three matter fermion generations. Each generation consists of five different representations of the gauge group:

$$(1, 2, -\frac{1}{2}), (3, 2, \frac{1}{6}), (1, 1, -1), (3, 1, \frac{2}{3}), (3, 1, -\frac{1}{3}), \tag{2.2}$$

where the numbers in parenthesis represent the corresponding charges under the group in Eq.(2.1). The matter content is shown in Table(2.1), The model also contains a single Higgs boson doublet, $\phi$ with charges (1, 2, 1/2), whose vacuum expectation value breaks the gauge symmetry,

$$< \phi >= \begin{pmatrix} 0 \\ \frac{v}{\sqrt{2}} \end{pmatrix} \Rightarrow G_{SM} \rightarrow SU(3)_c \times U(1)_{EM}. \tag{2.3}$$

This is the only piece of the SM which still misses experimental confirmation. Indeed, the search for the Higgs boson remains one of tasks of CMS [17] and ATLAS [18] experiments at LHC.

Table 2.1: The matter contents of the Standard Model

| $L_L$ (1,2,-1/2) | $Q_L$ (3,2,1/6) | $E_R$ (1,1,-1) | $U_R$ (3,1,2/3) | $D_R$ (3,1,-1/3) |
|---|---|---|---|---|
| $\begin{pmatrix} \nu_{eL} \\ e_L \end{pmatrix}$ | $\begin{pmatrix} u_L \\ d_L \end{pmatrix}$ | $e_R$ | $u_R$ | $d_R$ |
| $\begin{pmatrix} \nu_{\mu L} \\ \mu_L \end{pmatrix}$ | $\begin{pmatrix} c_L \\ s_L \end{pmatrix}$ | $\mu_R$ | $c_R$ | $s_R$ |
| $\begin{pmatrix} \nu_{\tau L} \\ \tau_L \end{pmatrix}$ | $\begin{pmatrix} t_L \\ b_L \end{pmatrix}$ | $\tau_R$ | $t_R$ | $b_R$ |

The neutrinos are fermions that have neither strong nor electromagnetic interactions. The SM has three active neutrinos accompanying the charged lepton mass eigenstates, e, $\mu$ and $\tau$. Neutrino interactions depending on the boson exchange are classified in two categories: the neutral current (NC) interactions exchanging the $Z^0$ mediator while interacting and the charged current (CC) interactions exchanging the $W^+, W^-$ bosons within interaction process. When a W is exchanged, charge conservation at the vertex requires that a charged lepton is emitted in the interaction. We know the family of an incoming neutrino by the charged partner which is emitted in the CC interaction. For example, a scattered electron tags a $\nu_e$ interaction, a muon tags a $\nu_\mu$ interaction, and a tau tags a $\nu_\tau$ interaction. The neutrino always emits the $W^+$ and the antineutrino always emits the $W^-$ in the CC interaction. At present the measurement of the invisible Z width yields $N_\nu = 2.984 \pm 0.008$ [19] which implies that there are only three light active neutrinos.

An important feature of the SM, which is relevant to the question of the neutrino mass, is the fact that the SM with the gauge symmetry of Eq.(2.1) and the particle content of Table (2.1) presents a global symmetry:

$$G_{SM}^{global} = U(1)_B \times U(1)_{L_e} \times U(1)_{L_\mu} \times U(1)_{L_\tau}, \tag{2.4}$$

$U(1)_B$ is the baryon number symmetry, and $U(1)_{L_e,L_\mu,L_\tau}$ are the three lepton flavor symmetries, with total lepton number given by $L = L_e + L_\mu + L_\tau$.

In summary, the neutrino interacting with the nature only via the weak interaction is a member of the Standard Model fermions and it is defined in the SM as neutral, massless and left-handed particle. In order to add a mass to the neutrino the SM has to be extended.

## 2.3 The Neutrino Oscillations

In 1957, Pontecorvo proposed oscillations between neutrinos and anti-neutrinos. The oscillations of neutrinos into anti-neutrinos were introduced in analogy to the oscillations between the neutral kaons $K^0$ and $\overline{K^0}$ [20]. After the discovery of the muon neutrino, the mixing of two massive neutrinos was introduced by Maki, Nakagawa, and Sakata [21] in 1962. By 1967, Pontecorvo and Gribov published a paper including a phenomenological theory for the oscillations between $\nu_e$ and $\nu_\mu$ [22]. The effect of matter on neutrino oscillations was first discussed by Wolfenstein and then carefully organized by Mikheyev and Smirnov [23].

### 2.3.1 The Neutrino Oscillations in Vacuum

The massive neutrinos indicate a spectrum of neutrino mass eigenstates in the 3-flavor neutrino oscillation framework as $\nu_i$, $i = 1, 2, 3$ each with a mass $m_i$. After a $\nu_\alpha$ ($\alpha$ here stands for leptons: $e, \mu$ and $\tau$) neutrino is produced together with a charged lepton, it travels a distance L to a detector. Its interaction occuring inside detector causes a second charged lepton tagging itself a second type neutrino, $\nu_\beta$. The changing the neutrino flavor from $\nu_\alpha$ to $\nu_\beta$ is a quantum-mechanical effect. In this case, the change of neutrino flavor is expressed by the the flavor-change probability, $P(\nu_\alpha \rightarrow \nu_\beta)$. The neutrino state emitted in $W^+$ decay together with the particular charged lepton is stated as

$$|\nu_\alpha\rangle = \sum_{i=1}^{3} U^*_{\alpha i} |\nu_i\rangle, \tag{2.5}$$

where, $U_{\alpha i}$ is the unitary leptonic mixing matrix. A superposition of flavors can be written for each mass eigenstates as:

$$|\nu_i\rangle = \sum_{\alpha=1}^{3} U_{\alpha i} |\nu_\alpha\rangle. \tag{2.6}$$

After its journey taking a distance L to the detector, the neutrino interacts with detector and a second charged lepton $\ell_\beta$ of flavor $\beta$ is produced by the weak

interaction. As a result, it can be said that the neutrino oscillates from $\nu_\alpha$ to $\nu_\beta$.

The oscillation amplitude $Amp(\nu_\alpha \to \nu_\beta)$ depends on three factors. The first one is the amplitude $(U^*_{\alpha i})$ for the neutrino produced by the source. The second one is the amplitude $Prob(\nu_i)$ for the produced $\nu_i$ to propagate from source to the target. The other is the amplitude $(U_{\beta i})$ for the charged lepton caused by the $\nu_i$ while it interacts with a target. The oscillation amplitude is a product of these three amplitudes, it can be written as

$$Amp(\nu_\alpha \to \nu_\beta) = \sum_i U^*_{\alpha i} Prob(\nu_i) U_{\beta i}. \tag{2.7}$$

Let's now find the probability Prob($\nu_i$) in $\nu_i$ rest frame. In this frame time is called as $\tau_i$. If $\nu_i$ has rest mass $m_i$, then in its rest frame its state vector obeys the Schrödinger equation.

$$i\frac{\partial}{\partial \tau_i}|\nu_i(\tau_i)\rangle = m_i|\nu_i(\tau_i)\rangle. \tag{2.8}$$

After solving the equation, we obtain

$$|\nu_i(\tau_i)\rangle = e^{-im_i\tau_i}|\nu_i(0)\rangle. \tag{2.9}$$

In order to find the Prob($\nu_i$), we should express the laboratory frame variables: L is the distance from the source that neutrino is produced to the detector neutrino interaction happens and $t$ is elapsed time during the trip. The value of $L$ is chosen by the experimenters through their choices for the location of the source and the location of the detector as seen in the OPERA experiment. $E_i$ and $p_i$ are the energy and momentum of the mass eigenstates $\nu_i$, respectively in the laboratory frame. By Lorentz invariance, the phase $m_i\tau_i$ in the $\nu_i$ propagator Prob($\nu_i$) is given in terms of the laboratory-frame variables by

$$m_i\tau_i = E_i t - p_i L. \tag{2.10}$$

Assuming that, $m_i^2 \ll E^2$ for any realistic energy E , $p_i$ can be written as

$$p_i = \sqrt{E^2 - m_i^2} \simeq E - \frac{m_i^2}{2E}, \tag{2.11}$$

at energy E the phase $m_i\tau_i$ in Prob($\nu_i$) is given by

$$m_i\tau_i \simeq E(t-L) + \frac{m_i^2}{2E}L. \tag{2.12}$$

In this expression, the phase E(t - L) is irrelevant since it is common to all the interfering mass eigenstates, and $t \approx L$ (L=ct, assuming $\hbar = c = 1$)in relativistic manner. Finally

$$Prob(\nu_i) = exp[-im_i^2\frac{L}{2E}]. \tag{2.13}$$

As a result, Neutrino oscillation amplitude in vacuum can be stated as follows:

$$Amp(\nu_\alpha \to \nu_\beta) = \sum_i U^*_{\alpha i} exp[-im_i^2\frac{L}{2E}]U_{\beta i}. \tag{2.14}$$

The oscillation probability $Prob(\nu_\alpha \to \nu_\beta)$ is

$$\begin{aligned} Prob(\nu_\alpha \to \nu_\beta) &= |Amp(\nu_\alpha \to \nu_\beta)|^2 = \delta_{\alpha\beta} \\ &\quad -4\sum_{i>j} \Re(U^*_{\alpha i}U_{\beta i}U_{\alpha j}U^*_{\beta j}) \sin^2(\Delta m^2_{ij}\frac{L}{4E}) \\ &\quad +2\sum_{i>j} \Im(U^*_{\alpha i}U_{\beta i}U_{\alpha j}U^*_{\beta j}) \sin(\Delta m^2_{ij}\frac{L}{2E}), \end{aligned} \tag{2.15}$$

where

$$\Delta m^2_{ij} \equiv m_i^2 - m_j^2. \tag{2.16}$$

and L is in km and E in GeV. Assuming $\hbar = c = 1$, we obtain

$$\Delta m^2_{ij}(\frac{L}{4E}) \simeq 1.27\Delta m^2_{ij}(eV^2)\frac{L(km)}{E(GeV)} \tag{2.17}$$

The unitary mixing matrix is parametrized as

$$U = \begin{pmatrix} c_{12}c_{13} & s_{12}c_{13} & s_{13}e^{-i\delta CP} \\ -s_{12}c_{23} - c_{12}s_{13}s_{23}e^{i\delta CP} & c_{12}c_{23} - s_{12}s_{13}s_{23}e^{i\delta CP} & c_{13}s_{23} \\ s_{12}s_{23} - c_{12}s_{13}c_{23}e^{i\delta CP} & -c_{12}s_{23} - s_{12}s_{13}c_{23}e^{i\delta CP} & c_{13}c_{23} \end{pmatrix},$$

where $c_{ij} \equiv \cos\theta_{ij}$ and $s_{ij} \equiv \sin\theta_{ij}$. The angles $\theta_{ij}$ are the mixing angles. The phases $\delta_{CP}$, $\eta_i\epsilon[0, 2\pi]$ are the CP violating phases. Here $\eta_i\epsilon[0, 2\pi]$ can be written as $\eta_1$ and $\eta_2$, and they are called also as Majonara phases.

The following equation expresses the oscillation probability and it is used in many neutrino oscillation experiments,

$$Prob(\nu_\alpha \rightarrow \nu_\beta) = sin^2 2\theta sin^2(1.27\Delta m^2(eV)\frac{L(km)}{E(GeV)}). \tag{2.18}$$

In the 3-flavor neutrino oscillation framework and $\Delta m^2_{12} \ll \Delta m^2_{23} = \Delta m^2_{13} = \Delta m^2$, the oscillation probabilities are stated as

$$Prob(\nu_\mu \rightarrow \nu_\tau) = cos^4\theta_{13} sin^2 2\theta_{23} sin^2(1.27\Delta m^2(eV)\frac{L(km)}{E(GeV)}), \tag{2.19}$$

$$Prob(\nu_\mu \rightarrow \nu_e) = sin^4\theta_{13} sin^2 2\theta_{13} sin^2(1.27\Delta m^2(eV)\frac{L(km)}{E(GeV)}), \tag{2.20}$$

$$Prob(\nu_\mu \rightarrow \nu_\mu) = 1 - Prob(\nu_\mu \rightarrow \nu_\tau) - Prob(\nu_\mu \rightarrow \nu_e), \tag{2.21}$$

where $\Delta m^2$ and $\theta_{23}$ is responsible for the dominant atmospheric oscillation: $\nu_\mu \rightarrow \nu_\tau$. On the other hand, the mixing angle $\theta_{13}$ is used for the sub leading $\nu_\mu \rightarrow \nu_e$ oscillation at the atmospheric scale.

### 2.3.2 The Neutrino Oscillations in Matter

The Neutrino oscillation probability is shaped when the neutrino faces with a matter. Beside the neutrino oscillation in vacuum, the matter effects on neutrinos were first explored for the neutrino oscilations in the sun by Mikheyev, Smirnov and Wolfenstein. Therefore, we can call the matter effects as MSW effects [24]. In general, matter effects arise in neutrino-electron scattering. The electron neutrino flavor experiences both (CC) and (NC) elastic forward-scattering with electrons. However, the $\nu_\mu$ and $\nu_\tau$ experience only NC forward-scattering, because creation of the $\mu$ or $\tau$ is kinematically forbidden or suppressed (e.g. $\nu_\mu + e^- \rightarrow \nu_e + \mu^-$). This difference produces the matter effect.

If $V_e$ is the elastic forward scattering potential for the $\nu_e$ component, and $V_{other}$ is the potential for the other neutrino flavors, then the additional scattering potential is

$$V = V_e - V_{other} = \sqrt{2} G_F n_e, \tag{2.22}$$

where $G_F$ is the Fermi constant and $n_e$ is the electron density. This potential modifies the Hamiltonian, so that, if $H_0$ is the vacuum Hamiltonian, then in matter the Hamiltonian is $H_0 + V$. This means that the eigenstates are modified from those of a vacuum, $\nu_1$ and $\nu_2$, to $\nu_{1m}$ and $\nu_{2m}$. Effectively, the neutrino mass spectrum is not the same as in vacuum. The solutions to the Hamiltonian are also modified. From this, one can see that the presence of electrons may substantially change the oscillatory behavior of neutrinos.

The simplest outcome is that matter induces a shift in the mass state, which is a combination of flavor eigenstates that propagates through the material. This leads to a change in the oscillation probability:

$$Prob(\nu_e \rightarrow \nu_\mu) = (sin^2 2\theta / W^2) sin^2(1.27 W \Delta m^2 \frac{L}{E}), \tag{2.23}$$

where $W^2 = sin^2 2\theta + (\sqrt{2} G_F n_e (2E/\Delta m^2) - cos 2\theta)^2$. One can see that if a neutrino, passing through matter, encounters an optimal density of electrons, a resonance, or large enhancement of the oscillation probability, can occur. The sun has a wide range of electron densities and thus is a prime candidate for causing matter effects. Also, neutrinos traveling through the Earth's core, which has a high electron density, might experience matter effects. This will produce a day-night effect or siderial variation, for neutrinos from the sun.

## 2.4 The Neutrino Oscillation Experiments

The oscillation parameters, a mixing angle $\theta$ and the mass-squared difference $\Delta m^2$, are measured with known neutrino path length $L$ and energy $E$ in neutrino oscillation experiments. If there is no mixing ($\theta = 0$) or $\Delta m^2 \ll 1$, the oscillation probability becomes zero, in this case, neutrino oscillation becomes meaningless.

There are two ways to detect neutrino oscillations of $\nu_\alpha \rightarrow \nu_\beta$. The first technique is to detect $\nu_\beta$ in a known neutrino flux of $\nu_\alpha$, which is known as the "appearance" of $\nu_\beta$. For example, in a test of oscillation hypothesis, $\nu_\mu \rightarrow \nu_\tau$ is

detected in the $\nu_\mu$ flux, as detected in the OPERA Experiment. Since neutrinos are observed by detecting the charged lepton produced in their CC interactions, they must have sufficient energy to produce the lepton. Thus, the energy of $\nu_\tau$ must be greater than 3.5 GeV to produce $\tau$-leptons through $\nu_\tau$ interactions with a fixed target nucleon. We would then look for $\tau$-lepton events.

The second technique is to observe "disappearance", where the detected neutrino flux of $\nu_\alpha$ is less than the expected flux in the absence of oscillations. In the previous example of $\nu_\mu \rightarrow \nu_\tau$ oscillations, if the energy of $\nu_\tau$ is less than the threshold of $\tau$-lepton production, instead of the observation of $\nu_\tau$, the depletion of $\nu_\mu$ would be an evidence for such oscillations.

A number of experiments and observations to search for neutrino oscillation have been performed around the world. They are categorized into four types according to their source of neutrinos; atmospheric neutrino observations, solar neutrino observations, reactor neutrino experiments, and accelerator neutrino experiments.

### 2.4.1 Atmospheric Neutrino Experiments

The first evidence of neutrino oscillations were presented by the Super-Kamiokande data for atmospheric neutrinos in 1998 [25]. Atmospheric neutrinos are produced in the Earth's atmosphere when it is hit by cosmic rays [26]. A very common product in these collisions are charged pions $\pi^\pm$ which decay as

$$\pi^\pm \longrightarrow \mu^\pm + \overline{\nu_\mu}(\nu_\mu).$$

The resulting $\mu^\pm$ from this decay then subsequently decay according to

$$\mu^\pm \longrightarrow e^\pm + \overline{\nu_\mu}(\nu_\mu) + \overline{\nu_e}(\nu_e).$$

For low energies ($E_\mu < 5GeV$), the $\mu^\pm$ will decay before it hits the ground. Thus, at these energies, the ratio $R_{\frac{\nu_\mu}{\nu_e}}$ between the number of muon neutrinos and the

number of electron neutrinos will be two as the above decay chain produces two muon neutrinos and one electron neutrino. At higher energies, the $\mu^{\pm}$ will hit the Earth's surface and stop before it has had time to decay. As a result, the relative number of electron neutrinos produced at these high energies will decrease, resulting in a higher value of $R_{\frac{\nu_\mu}{\nu_e}}$. Although atmospheric neutrinos had been studied by several earlier experiments [27, 28], Super-Kamiokande was the first to provide evidence of neutrino oscillations [25]. In the Super-Kamiokande experiment, the $\nu_e$ and $\nu_\mu$ fluxes were measured at different zenith angles, corresponding to different path lengths from production to detection. Following the Super-Kamiokande results, oscillations of atmospheric neutrinos have also been observed by the SOUDAN-2 collaboration [29].

### 2.4.2 Solar Neutrino Experiments

Since the Sun produces its energy via thermonuclear reactions, it is said to be a source of neutrinos. The neutrinos, beside the electromagnetic waves and solar wind, can provide us information about the center of the Sun. The Standard Solar Model (SSM) [30, 31, 32] has been very successful in describing the composition, energy production, and seismology of the Sun. It also gives information about what the neutrino flux would be. The most abundant fusion reaction in the Sun is as the following:

$$p + p \longrightarrow^2 H + e^+ + \nu_e,$$

which produces the large $pp$ flux at $E < 0.4$ MeV. The first experiment by which the solar neutrino flux was measured was the Homestake experiment [33]. It used inverse beta-decay

$$\nu_e + ^{37} Cl \longrightarrow ^{37} Ar + e^-,$$

in a 400 $m^3$ tank of perchloroethylene, essentially cleaning fluid, where the produced Argon atoms were then counted by radiochemical means. The result of

the experiment was that the number of Argon atoms was lower than what was expected from the SSM, this observation became known as the solar neutrino problem. One of the solution of this problem is that electron neutrinos are lost somewhere along the propagation from the Sun to the Earth. It would be an indication of neutrino oscillations or some other flavor transition mechanism. One of the drawbacks of the Homestake experiment was that its threshold energy of about 0.9 MeV was above the energy of the large flux of *pp* neutrinos, and thus, it was sensitive only to neutrino fluxes with larger uncertainties. This drawback was addressed in the Gallium experiments GALLEX [34, 35] and SAGE [36, 37], which both used a method very similar to that of the Homestake experiment. Instead of detecting the inverse beta-decay of Chlorine, these experiments relied on the inverse beta-decay of Gallium.

$$\nu_e + {}^{71}Ga \longrightarrow {}^{71}Ge + e^-,$$

The results of the Gallium experiments were the same as that of the Homestake experiment, a deficiency in the flux of electron neutrinos from the Sun. A second drawback of the Homestake experiment, which was shared by the Gallium experiments, was that there was no directional information for the inverse beta-decays. This drawback is not present in water Cherenkov detectors such as Kamiokande [38] and Super-Kamiokande [39]. These detectors can detect solar neutrinos by the Cherenkov light in water produced by electrons which have undergone elastic scattering

$$\nu_e + e^- \longrightarrow \nu_e + e^-,$$

the water Cherenkov technique measures the events in real-time and the direction of the scattered electron gives some information on the direction of the incoming neutrino. In fact, the measurement of the directionality of neutrinos in the Kamiokande was the first proof that the neutrinos were actually originating from the Sun [40]. The resolution to the solar neutrino problem came with the results

of the Sudbury Neutrino Observatory (SNO) [41] which uses methods similar to the water Cherenkov detectors. However, instead of the detector volume being filled with ordinary water, it is filled with heavy water. With the presence of deuterium in the detector, CC

$$\nu_e + D \longrightarrow p + p + e^-,$$

and NC

$$\nu_e + D \longrightarrow n + p + \nu_e,$$

reactions are allowed, making it possible to detect neutrinos also through these reactions. While the CC reaction is only sensitive to electron neutrinos, the cross-section for the NC reaction is independent of the neutrino flavor. Thus, the SNO was able to measure both the flux of electron neutrinos and the total flux of neutrinos independently. The conclusion from this is that the electron neutrinos produced in the Sun change their flavor during their propagation to the Earth.

### 2.4.3 Reactor Neutrino Experiments

Through the decays that follow the fission processes in a nuclear reactor, nuclear power plants become an abundant source of artificial low-energy anti-neutrinos with well-known energy spectra. Thus, it becomes natural to try to study the oscillations of these anti-neutrinos. In principle, there are two types of reactor neutrino oscillation experiments. The short-baseline experiments such as CHOOZ [42] and Palo Verde [43], where the detectors are placed relatively close to the reactor, are trying to find the oscillations associated with the large mass squared difference $\Delta m^2_{31}$, where the oscillations governed by $\Delta m^2_{21}$ have not yet had time to develop. Such experiments are mainly sensitive to the small mixing angle $\theta_{13}$ since, for $\Delta m^2_{21} \to 0$,

$$P_{ee} = 1 - sin^2(2\theta_{13}) sin^2(\frac{\Delta m^2_{31}}{4E} L), \tag{2.24}$$

and the absolute value of $\Delta m^2_{31}$ is fairly well known from atmospheric neutrino oscillations. In fact, the current upper bound on $\theta_{13}$ comes from the CHOOZ experiment [42] which was a short-baseline reactor neutrino experiment, along with external bounds on $\Delta m^2_{31}$.

In addition to the short-baseline reactor neutrino experiments, there is also the possibility to detect reactor neutrinos at longer distances, it is called long-baseline reactor neutrino experiments. The detector should be placed at about equal distance from a number of nuclear power plants, which will all generate neutrinos that can be detected. The Kamioka site is located at about 180 km away from a large number of nuclear power plants in Japan and Korea and the Kamioka Liquid Scintillator Anti-Neutrino Detector (KamLAND) [44] is detecting the reactor neutrinos coming from these power plants. As in the case of the Super-Kamiokande experiment, the L/E behavior in KamLAND has been studied and compared to the predictions of neutrino oscillations and other mechanisms of neutrino flavor transition [44].

### 2.4.4 Long Baseline Accelerator Experiments

In this section, we will deal with accelerator neutrino experiments. One of the great advantages of using accelerator neutrinos lies in the fact that the entire experiment can be completely designed and controlled by physicists. Complications in the analysis results from the difficulty in understanding the production of atmospheric neutrinos (affecting the understanding of $E$) and in the accurate reconstruction of events as a function of zenith angle (affecting knowledge of $L$). The $\Delta m^2(eV^2)$ obtained from the Kamiokande data is an order of magnitute much more than that obtained from the Super-K data. Thereby, it was crucial for accelerator long-beamline neutrino experiments to confirm this result. Since some challenges for long-baseline experiments are required, these challenges have

been overcome by KEK, FNAL and CERN. By making these accelerator long-baselines, the first confirmation of the atmospheric neutrino deficit came from the KEK-to-Kmiokande(K2K) long baseline experiment [45, 46, 47]. The K2K experiment had an initial beam of muon neutrinos and studied the disappearance of these muon neutrinos. In this experiment, the likelihood was maximized in the $\Delta m^2$ ,$sin^2 2\theta$ space and the best fit point within the physical region was found to be at $\Delta m^2 = 2.8 \times 10^{-3}(eV^2)$ and $sin^2 2\theta = 1.0$. The highest likelihood was found $\Delta m^2 = 2.6 \times 10^{-3}(eV^2)$ and $sin^2 2\theta = 1.2$. K2K compares the results with the parameters found by the measurement of atmospheric neutrino oscillation by the Super-Kamiokande collaboration [3]. The allowed regions of oscillation parameters found in the analysis together with SK result are shown in Figure(2.1).

K2K result was in good agreement with the parameters found using atmospheric neutrinos. The K2K experiment has been followed up by the MINOS experiment [48] to high precision. The last data obtained were consistent with $\nu_\mu$ disappearance via oscillations with $\Delta m^2_{32} = 2.74^{+0.44}_{-0.26} \times 10^{-3} eV^2/c^4$ and $sin^2(2\theta_{23}) > 0.87(68\% CL.)$. The resulting 68% and 90% confidence intervals are shown in Figure (2.2).

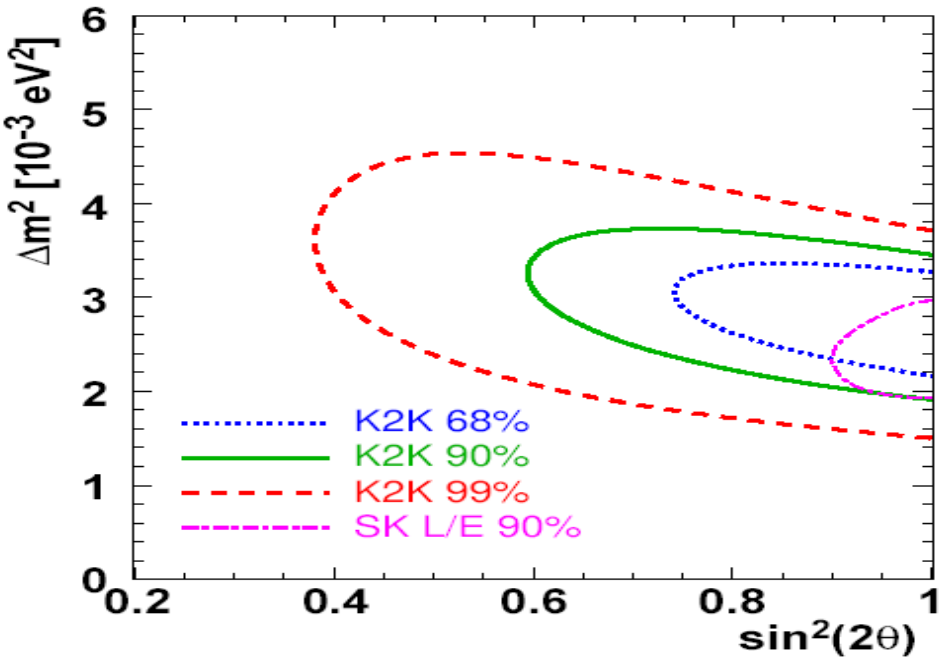


Figure 2.1: Comparison of K2K results with the SK atmospheric neutrino measurement. Dotted, solid, dashed, and dash-dotted lines represent 68%, 90%, 99%, 90% CL. Allowed regions of K2K and 90% CL. Allowed region from SK atmospheric neutrino, respectively.

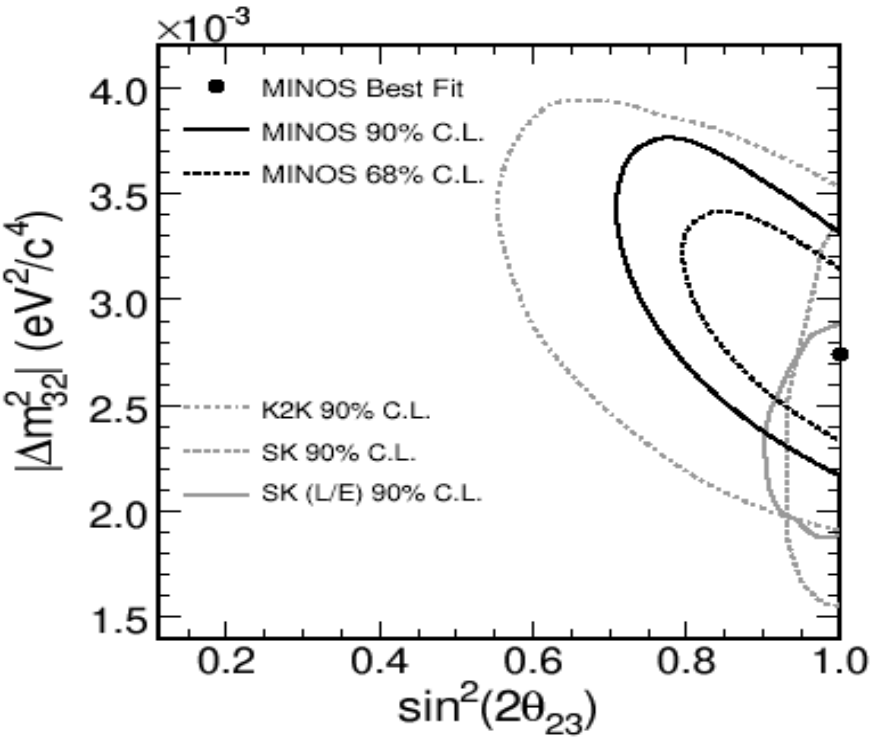


Figure 2.2: Allowed regions of the MINOS. Comparison of the MINOS results with the long-baseline K2K experiment and the SK atmospheric neutrino measurement.

# CHAPTER 3

# THE OPERA EXPERIMENT

## 3.1 Introduction

OPERA [4] is a long-baseline neutrino experiment located at the Gran Sasso Labaratory, 732 km from CERN. The OPERA Experiment is designed and optimised for a direct appearance search of $\nu_\mu \rightarrow \nu_\tau$ oscillations in the parameter region indicated by Super-Kamiokande [2] in explanation of the zenith dependence of the atmospheric neutrino deficit. It detects the $\nu_\tau$ CC interactions in almost pure muon neutrino beam produced at CERN SPS. In addition to $\nu_\mu \rightarrow \nu_\tau$ oscillations, the OPERA detector will also be searching for $\nu_\mu \rightarrow \nu_e$ oscillations; thanks to its electron identification capability. The OPERA detector, a large detector (10m×10m×20m), is made of two identical super-modules (SMs) each consisting of a target section and a muon spectrometer as shown in Figure (3.1). The (ECC), a part of the target section, is a modular structure made of a sandwich of passive material plates interspaced with emulsion layers. By assembling a large quantity of such modules, it is possible to conceive and realize 1500 ton fine-grained vertex detector optimized for the study of $\nu_\tau$ appearance. The target part is completed with magnetised iron spectrometers for muon charge and momentum measurements, and electronic detectors for event location inside the ECC Brick.

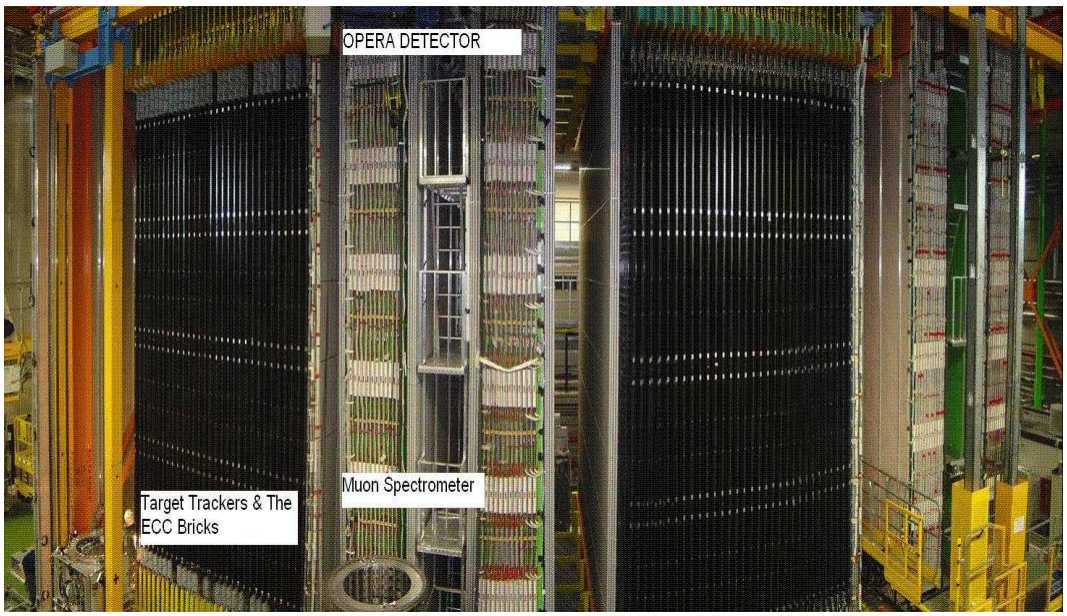


Figure 3.1: A schematic view of the OPERA detector. The super-modules are composed of a lead target combined with a scintillator target tracker and an electronic muon spectrometer.

## 3.2 The Neutrino Beam

The CNGS (from CERN to LNGS) [49] neutrino beam was optimized for $\nu_\tau$ appearance in the parameter region indicated by the atmospheric neutrino experiment [3]. The schematic view of the beam line can be seen in Figure (3.2). Before producing $\nu_\mu$, the Linac accelerates protons to an energy of 50 MeV. These protons are then injected to the Booster boosting the 50 MeV energy to 1.5 GeV, are then sent to the Proton Synchrotron (PS) where they reach an energy of 14 GeV before they are transferred to the Super Proton Synchrotron (SPS). Finally, the protons reach their final energy of 400 GeV. The schematic view of accelerator

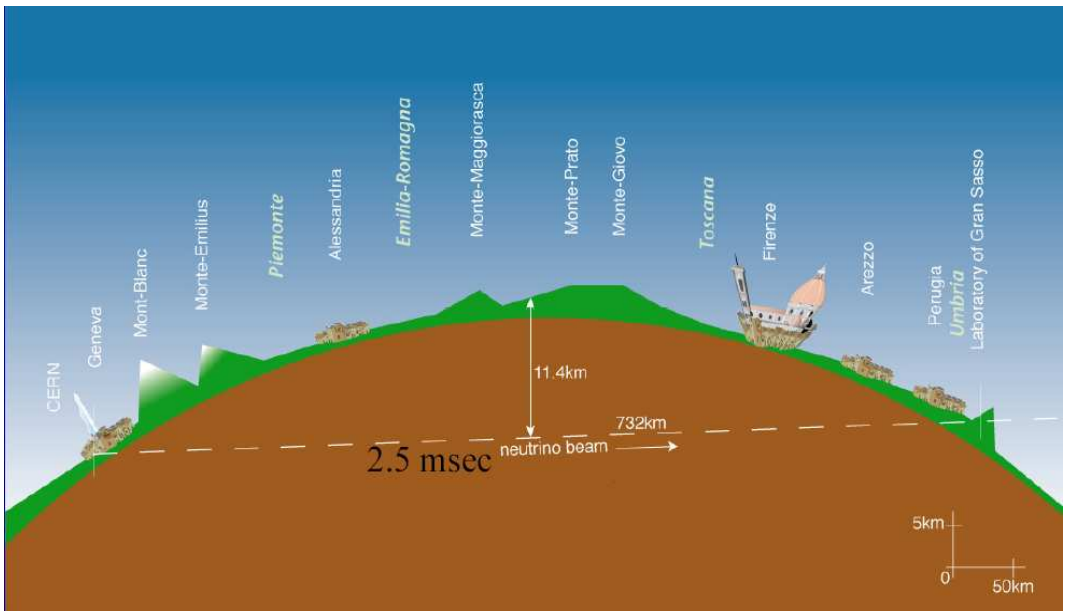


Figure 3.2: the CNGS beam line

complex of CERN is shown in Figure (3.3). A 400 GeV proton beam is extracted from the CERN SPS in 10.5 $\mu$s short pulses with design intensity of $2.4 \times 10^{13}$ protons on target (p.o.t) per pulse. The proton beam is transported through the transfer line TT41 to the CNGS target T40 [50]. The target consists of a series of thin graphite rods cooled with helium. Secondary pions and kaons of positive charge produced in the target are focused into a parallel beam by a system of two magnetic lenses, called horn and reflector. A 1000m long decay-pipe allows the pions and kaons to decay into muon-neutrinos and muons. The remaining hadrons (protons, pions, kaons, . . . ) are absorbed by an iron beam-dump. The muons are monitored by two sets of detectors downstream of the dump, where they measure the muon intensity, the beam profile and its centre.

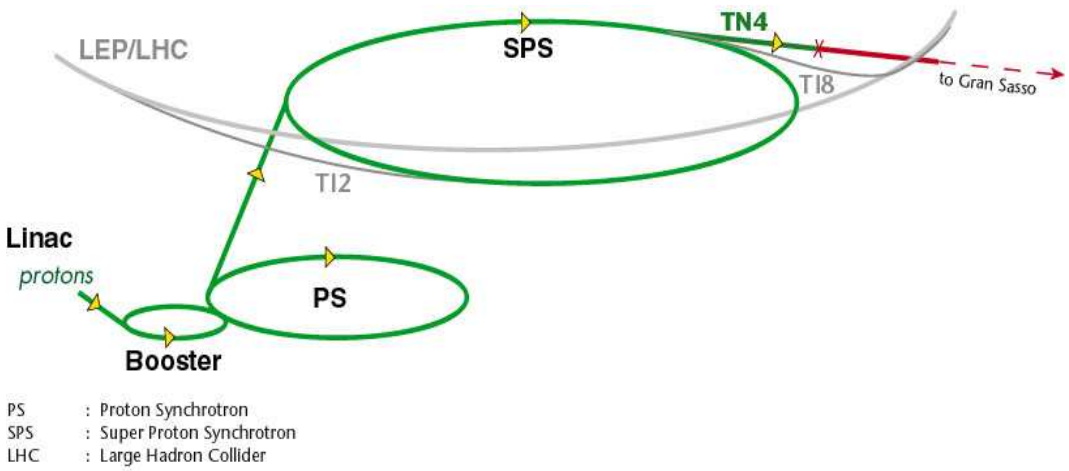


Figure 3.3: CERN accelerators to obtain 400 GeV protons.

Further downstream the muons are absorbed in the rock while neutrinos continue to travel towards Gran Sasso. As regards to the beam parameters, the average neutrino energy at the LNGS location is about 17GeV. The $\overline{\nu_\mu}$ contamination is about %2.1. The $\nu_e$ and $\overline{\nu_e}$ contaminations are lower than %1 while the number of prompt $\nu_\tau$ from $D_s$ decay is negligible. The average $(L/E_\nu)$ ratio is 43 km $GeV^{-1}$. Due to the Earth's curvature, neutrinos from CERN enter the LNGS halls with an angle of about $3^0$ with respect to the horizontal plane [49]. The horizontal plane of CNGS can be seen in Figure(3.4). The beam features are shown in Table (3.1).

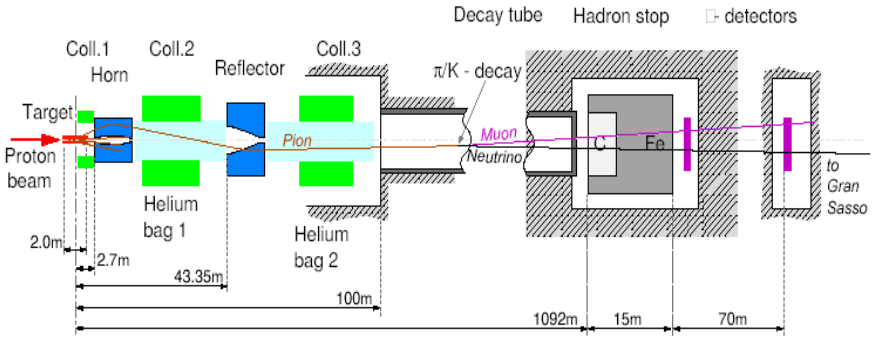


Figure 3.4: Horizontal plane of CNGS.

Table 3.1: The CNGS neutrino beam features.

| | |
|---|---|
| L | 732 km |
| $< E_\nu >$ | 17GeV |
| $L/ < E_\nu >$ | 43 km/GeV |
| $(\nu_e + \overline{\nu_e})/\nu_\mu$ | 0.87% |
| $\overline{\nu_\mu}/\nu_\mu$ | 2.1% |
| $\nu_\tau$ prompt | negligible |

## 3.3 Experimental Setup

The OPERA Detector located in hall C of the Gran Sasso, underground laboratory in Italy, combines the ECC with electronic detectors. This combined structure is called as "hybrid" detector. A schematic view of the OPERA detector is illustrated in Figure(3.1). The detector consists of two identical parts called Supermodules (SMs). The main parts of the SMs are a target part and a muon spectrometer [51].

The target part is composed of 31 walls (62 in total). Each wall contains a

layer called the "brick wall' and just behind it a second layer called the "TT wall". In each brick wall more than 75000 ECC bricks are placed. These bricks are composed of a stack of 56 layers of lead of a thickness of 1mm, interleaved with 43$\mu$m thick emulsion layers on both sides of a 205$\mu$m thick plastic base. These bricks are manipulated into brick wall with the help of the Brick Manipulation System (BMS) [49]. Beside ECC sheet, the Changable Sheet (CS) [52] is independently packed and placed downstream of each brick. The TT wall is composed of horizontal and vertical scintillator strips read out WLS fibres coupled to two 64-pixel photodetectors [53]. The muon spectrometer, as seen in Figure (3.1), consists of a dipole magnet made of 24 iron walls, 5cm thick, separated by a 2cm air gap. The iron plates are magnetized with a magnetic field intensity of 1.55T. The Resistive Plate Chambers (RPCs) allow to generate the prompt signal for the drift tubes electronics (the system used for high accuracy tracks reconstruction). The RPCs are embedded in the magnet iron plates: One RPC layer is made of 21 RPCs , arranged in a 3x7 matrix. Each detector plane is sandwiched between two polypropilene layer with pickup copper strips with horizontal (35 mm pitch) and vertical orientation (26 mm pitch), respectively [54]. After a neutrino interaction occurs in the target part, the candidate brick indicated by the TT is extracted, and then CS, at downstream face of the brick, is scanned and searched for interaction. If a charged particle trajectory is found in these emulsion sheets, the brick belonging to neutrino interaction vertex is exposed to cosmic rays for film alignment, and then disassembled. The emulsions are developed on-site and sent to participating laboratories for scanning. After scanning and data taking, particle track segments (microtracks) are analyzed and the event is reconstructed using momentum information from multiple coulomb scattering and readouts of the TT and the muon spectrometers.

### 3.3.1 The OPERA Films

In order to produce emulsion plates in large-scale applications and R&D project was carried out between the Fuji-Film company and Nagoya University in Japan [55]. A target mass of 1 kton requires an area of emulsion sheet having the order of 100.000 $m^2$. Because the production of this amount of film by hand is not possible, Fuji Film company has used some commercial machines in order to avoid time consuming production. The cross-sectional view of the OPERA emulsion film is shown in Figure (3.5). The emulsion sheet has been processed

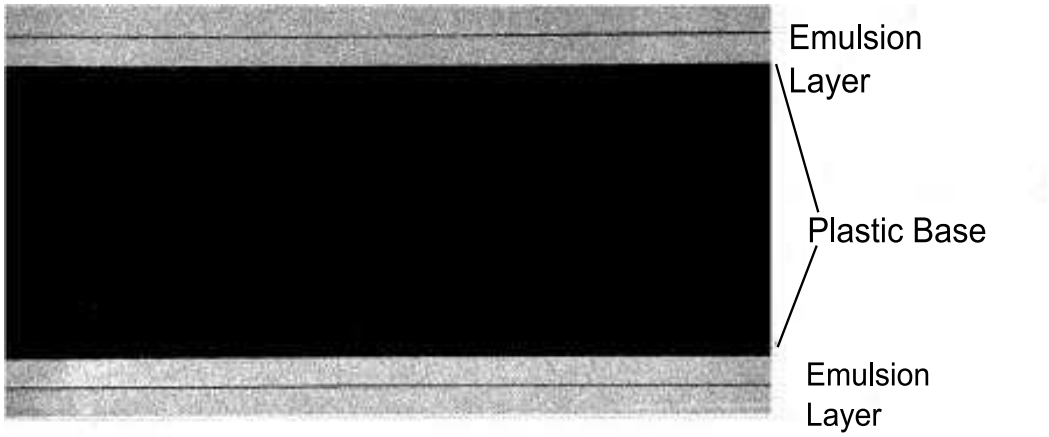


Figure 3.5: A cross-sectional view of the machine-coated OPERA film.

by pouring the gel on plastic plates and drying them in climate-controlled room. These procedures make plates different from each other. The thickness of the plastic base is 205 $\mu m$. Emulsion plates have been placed on both sides of the

base material. The black lines, middle of the emulsion layers, are protection coats with thickness of 1 $\mu m$. The OPERA emulsion layers are 43 micron thick. With the usage of the machine coating system, a productive layer was generated automatically on the emulsion film surface. The aim of the protective layer is to protect the active layer of the coated gel from any kind of mechanical affects. It also provides to avoid extra cleaning procedure for the emulsion films being exposed to lead effects inside ECC. The emulsion films get some spots after waiting in contact with lead. More detailed information about the lead effects inside the ECC brick is given by [56]. These spots are called "fog". They can be erased with a refreshing procedure. The OPERA emulsions are refreshed by applying high humidity and high temperature for 6 days. The optimum fog level for the films is 5 grains/1000$\mu m^3$.

### 3.3.2 Emulsion Cloud Chamber

The main components of the ECC are lead, 1mm thick, and emulsion films. The emulsion film consisting of two emulsion layers (44$\mu$m thick each) placed on either side of a plastic base (205$\mu$m thick) is inserted between lead plates. The ECC brick is made by the Brick Assembling Machine (BAM). The BAM assembles and produces the ECC bricks, weighting 8.3 kg, as a stack of 56 lead plates interleaved by 57 nuclear emulsion films. The transverse dimension of an ECC brick is 10.2cm×12.7cm; the thickness is 7.5 cm. This dimension corresponds to $\sim 10X_0$ radiation lengths, enough to allow electron identification via electromagnetic shower reconstruction in ECC and momentum measurements by multiple scattering. A schematic view of an assembled brick is shown in Figure (3.6). After the BAM produces the ECC brick, a special type of emulsion sheets called changeable sheet doublets are attached to the downstream face of each ECC brick. The CS provides to confirm the ECC brick which includes the

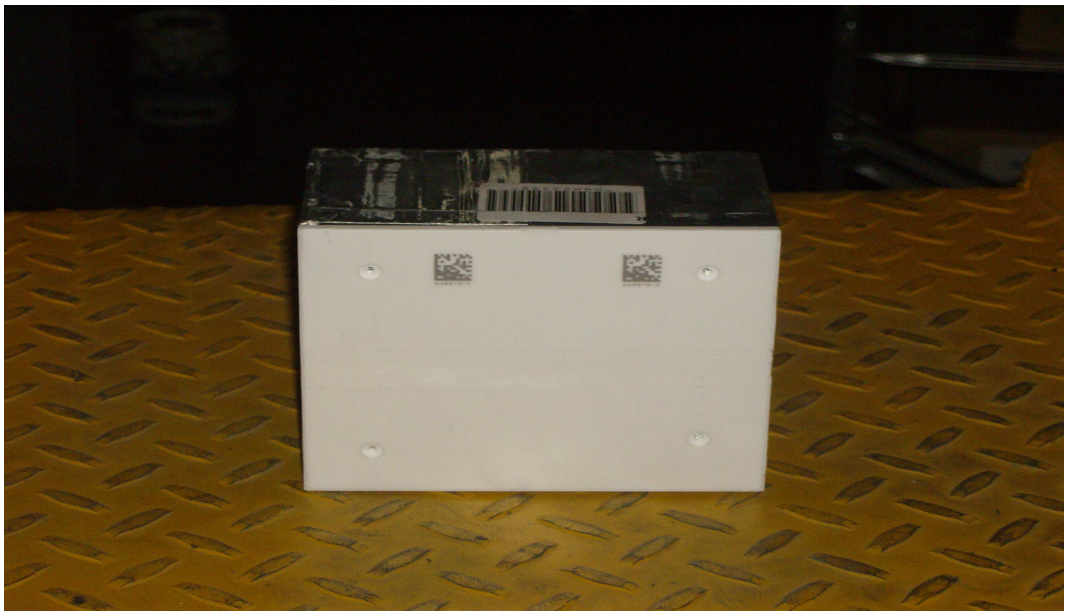

Figure 3.6: An assembled brick by BAM facility. It consists of 57 emulsion films and 56 leads inside. A CS doublet is attached to the downstream face of the ECC brick.

neutrino interaction vertex. It is useful to avoid useless film handling and processing of the misidentified bricks causing needless scanning overload of the ECC bricks [52].

### 3.3.3 Target Trackers

The electronic TT following the brick walls are composed of two planes oriented along the X and Y axis,respectively. These two planes are constituted by 4 modules and squares of $6.7 \times 6.7 m^2$ sensitive edge-to-edge surface. A schematic view of the target tracker planes are shown in Figure (3.7). A basic unit of

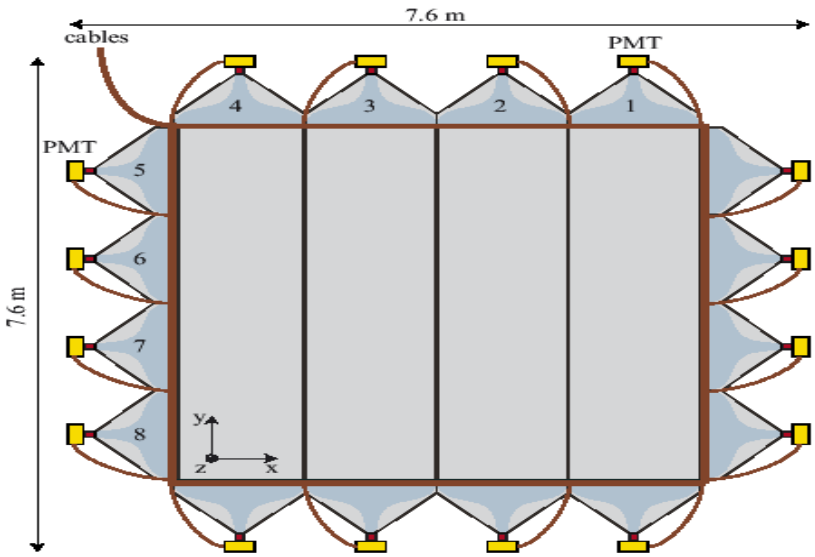


Figure 3.7: Target tracker planes oriented along the X and Y axis, respectively.

the module consists of 64 strips, 26.3 mm wide and 10.6 mm thick, readout by wavelength shifting (WLS) fibres coupled to two 64-pixel photodetectors. The two end-cabs of each target tracker module play an imortant role; they protect the WLS fibres emerging from the scintillating strips that are guided towards the input window of the multi-anode photomultipliers. They host the PM tubes as well as the monitoring light injection system, the front-end electronic cards and the HV power supplies. They also provide the mechanical structure by which the modules will be suspended on the OPERA detector. The schematic view of the end-cap of a scintillator strip module can be seen in Figure (3.8) [53].

The brick wall in front of the target tracker is a place where a neutrino interaction has happened. The trigger signal indicating the vertex location is obtained

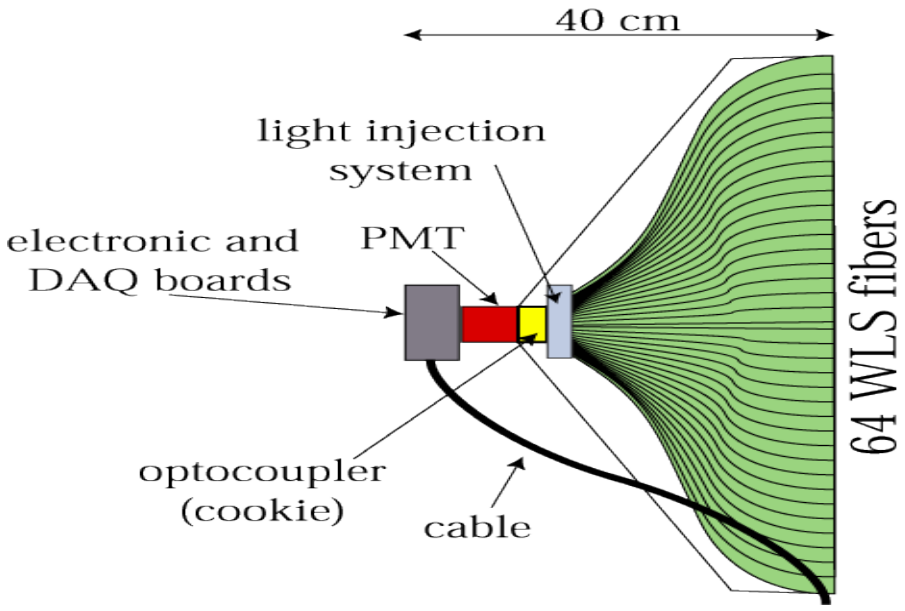


Figure 3.8: An end-cap of a scintillator strip module.

by electronic detectors and is used to remove candidate ECC brick where a neutrino interaction has taken place. Briefly, the target tracker provides information to find secondary particles obtained from the neutrino interaction in ECC brick and determines the related brick to be removed for reconstruction and analysis. The efficiency of the TT is about %70. As an example of the illustration of a decay channel reconstructed in the OPERA target, one can see the muonic decay of $\tau$ transverse to the z direction of the detector in Figure (3.9).

### 3.3.4 Emulsion Film Refreshing

Since the connection criteria between TT and the ECC bricks with respect to providing vertex localization inside the ECC is an important subject for the $\nu_\mu \rightarrow \nu_\tau$ oscillations, CSd sheets are used as interfaces between TT detectors

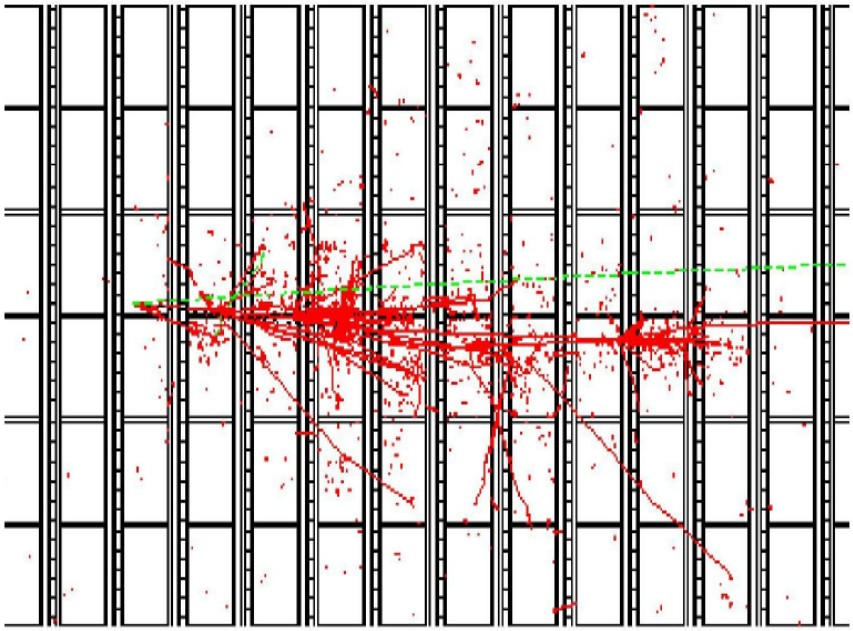

Figure 3.9: Illustration of the $\tau \rightarrow \mu$ decay in the OPERA target. The thin lines are TT, with strips and oriented X and Y planes, and thick lines are brick walls. The third brick walls can be seen as the primary vertex.

and the ECC bricks correponding to signal of electronic detectors [4]. The CS is composed of two nuclear emulsions packed in polyethylene-aluminum laminated envelope and installed inside plastic box as seen in Figure (3.10).

The CSd are placed to the downstream face of the ECC bricks. An illustration of the CSd localized between TT and the ECC brick is shown in Figure (3.11).

There are two aims of the CSd attached to the ECC bricks along the beam time, the first aim is to confirm the neutrino interaction signals obtained from TT detector. The other is to find neutrino-related interactions for the ECC brick

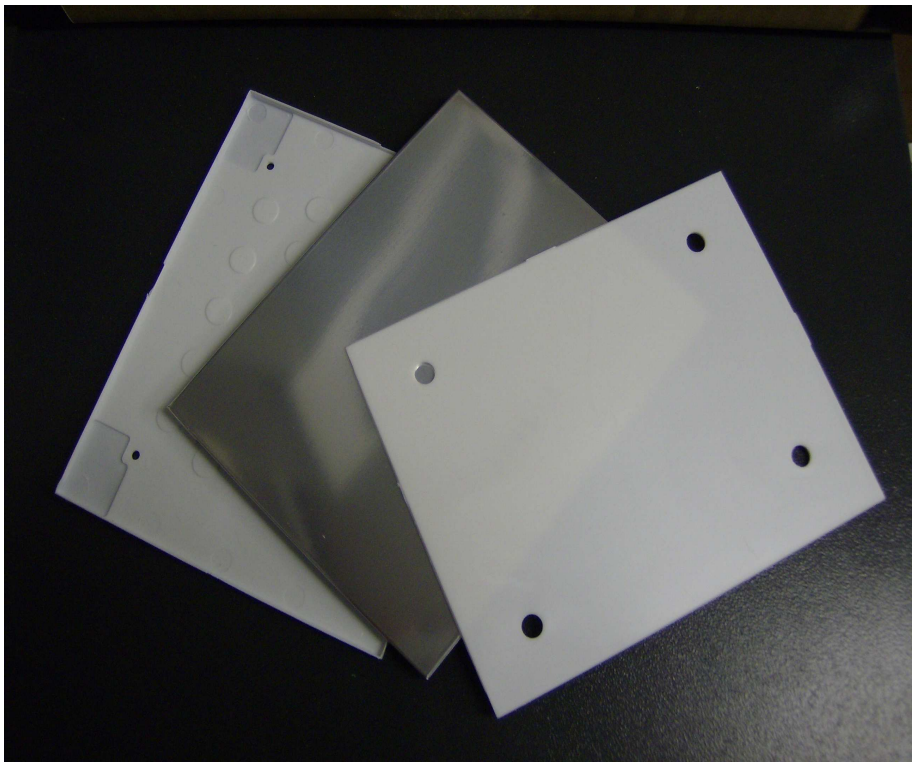

Figure 3.10: A schematic view of the CS being prepared for the ECC brick.

scan-back analysis [52]. These major roles of the CSd doublets provide to decrease useless scanning load, useless film handling and processing, and also to improve the location efficiency. These CS doublets are produced at the underground laboratory by applying some steps such as refreshing, packing, clinching and installing. Emulsion refreshing is a process that erase fog and cosmic rays (mainly during the transportation) in order to reset the emulsion history. This procedure is conducted by keeping emulsions in high humidity conditions in the chamber for 6 days. A facility was constructed in LNGS in order to refresh CS films before using. This work is under the responsibility of Japanese, Russian and Turkish

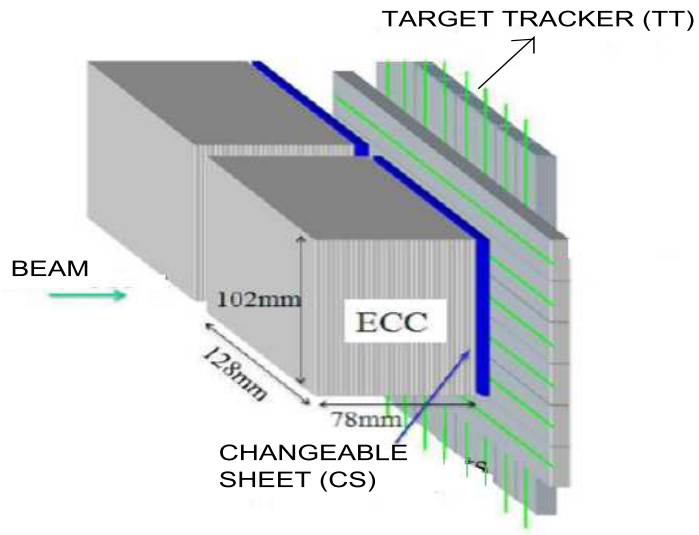


Figure 3.11: The basic demonstration of the Changeable Sheed Doublets (CSd) attached to the downstream of the ECC bricks and placed between TT and The ECC.

groups. METU group has contributed this work from the very beginning. More detailed information about the refreshing procedure applied for the emulsion films can be found in [55]. CSd must be vacuumed in order to keep the alignment during the experiment, and therefore they are packed in polyethylene-aluminum laminated envelope after refreshing step. CS packed inside envelope is clinched on its 3 sides in order to fix it inside the box. Finally, CS envelope clinched with the clinching machine is installed inside white box shown in Figure (3.10). About 346.000 emulsion films have been refreshed and packed since August 2005.

### 3.3.5 The Muon Spectrometer

A study of muonic $\tau$-channel is performed by using the muon spectrometers for identification of muons , for determination of their momentum and for detection their charge sign. It also helps for lowering background effects caused by the decay of charmed particles. The muon spectrometer is composed of a dipolar magnet consisting of two iron walls interleaved by pairs of high-resolution trackers (PT) [57]. Each wall is constituted by 12 iron plates 5cm thick and these plates are separated by 2cm gaps filled with Resistive Plate Chambers (RPC). The iron is magnetized with a magnetic field intensity of 1.55T by a current of about 1200A circulating in the top and bottom copper coils . The transverse dimensions of the magnets are 8.75 m horizontally, 8m vertically and 2.64m in length providing adequate geometrical acceptance also for muons originating in the upstream target volume. The magnets and the detectors (RPC planes and drift tubes) are organized to perform more precise muon momentum measurements and determine with higher accuracy their charge sign. Each RPC plane (inner tracker) covering a $70m^2$ surface is designed to operate in streamer mode. The design performances foresee a muon identification efficiency larger than %95 when the spectrometer information is joined to the target tracker one and a momentum resolution better than %20 below 50 GeV [58].

## 3.4 Physics Performances

### 3.4.1 The $\tau$-Detection in the OPERA Experiment

As soon as the $\nu_\tau$CC interaction happens in the brick wall, the $\tau$-lepton is produced. The detection of the $\tau$-lepton in the brick part will show the occurrence of $\nu_\mu \rightarrow \nu_\tau$ oscillation. The decay channels searched in ECC are the electron, muon and a single charged hadron channels. The tau-lepton decay channels are

shown as

$$\tau^- \longrightarrow e^- \nu_\tau \overline{\nu_e},$$

$$\tau^- \longrightarrow \mu^- \nu_\tau \overline{\nu_\mu},$$

$$\tau^- \longrightarrow (h^- h^+) h^- \nu_\tau (n\pi^0),$$

The branching ratio (BR) of these three single-prong decay modes are %17.8, %17.7 and %49.5 for the electronic, muonic and hadronic channels, respectively. There are two types of $\tau$ decays, short and long decays depending on the location of the $\tau$ decay vertex. In the short decay condition, the $\tau$ is produced by the $\nu_\tau$ interaction in the lead plate inside ECC, and then the $\tau$ decays in the same lead plate. In the long decay condition, the $\tau$ decays in a lead plate different from where it is produced [59]. The selection of the long decay events are based on the existence of a kink angle between the $\tau$ and the daughter tracks ($\theta_{kink} > 20mrad$). A schematic view of the long $\tau$ decay topology in ECC and the Emulsion Film design can be seen in Figure (3.12). The selection of the short decay events are based on the impact parameter of the $\tau$ daughter track with respect to the interaction vertex ($IP > 5 - 20\mu m$). The main background sources consist of charm decays (%54), hadron interactions (%30) and large angle muon scattering (%16). The detection of the $\tau$ decay channel into electron is provided by the dense structure of the ECC brick allowing to reconstruct electron shower efficiently. The main background to this channel comes from charm production in the $\nu_\mu$ CC interactions. The muon track from $\tau$ decay provides to localize the event. The main background to this channel is the large angle muon scattering in the lead plates. The topological cuts on the kink angle and on the transverse momentum of the muon helps to reduce the background signals. The $\tau$ decay channel into hadrons can be searched by its high branching ratio. Although These decay modes possess largest branching ratio with % 49.5, the hadronic reinteractions affect these hadronic decay modes negatively as a high background. The summary of

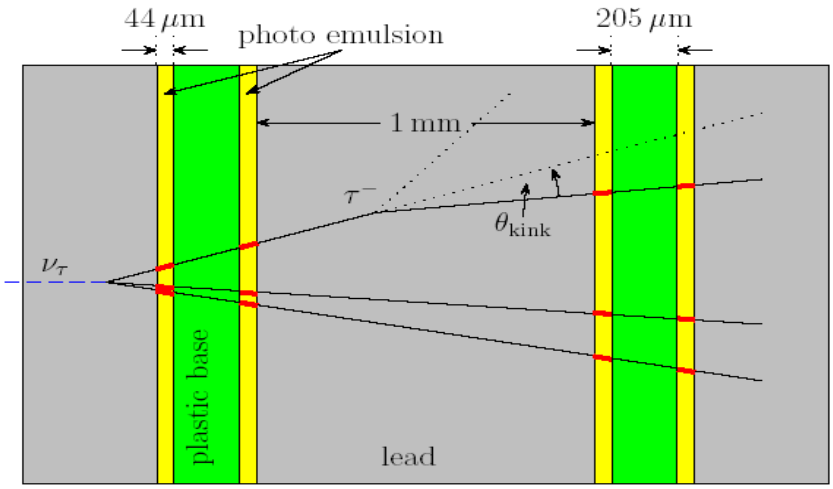


Figure 3.12: Emulsion cloud chamber having typical $\tau$-lepton decay topology.

the OPERA detector performance after 5 years of running is illustrated in Table (3.2).

The sensitivity of the OPERA experiment to $\nu_\mu \rightarrow \nu_\tau$ oscillation can be seen in Figure (3.13).

In addition to the dominant $\nu_\mu \rightarrow \nu_\tau$ oscillation, subleading transition involving $\nu_e$ may take place as well in a 3 flavours general framework. The $\nu_\mu \rightarrow \nu_e$ oscillation at the atmospheric scale ($\Delta m^2$) is driven by the mixing angle $\Theta_{13}$ which is constrained by CHOOZ experiment to be small ($\Theta_{13} < 11^0$ for $\Delta m^2 = 2.5 \times 10^{-3} eV^2$) [61]. The Table (3.3) summarizes the expected number of signal and background events in three family mixing and using the expected $\nu_e$ beam contamination.

Table 3.2: The summary of the expected numbers of the $\tau$ events and background events in 5 years of data taking. The signal for $\Delta m^2$ is compatible with the Super Kamiokande Results [60].

| Decay Channels | $\varepsilon(\%)$ | BR(%) | signal $\Delta m^2 = 2.5 \times 10^{-3} eV^2$ | signal $\Delta m^2 = 3.0 \times 10^{-3} eV^2$ | Bkg |
|---|---|---|---|---|---|
| $\tau \rightarrow \mu$ | 17.5 | 17.7 | 2.9 | 4.2 | 0.17 |
| $\tau \rightarrow e$ | 20.8 | 17.8 | 3.5 | 5.0 | 0.17 |
| $\tau \rightarrow h$ | 5.8 | 49.5 | 3.1 | 4.4 | 0.24 |
| $\tau \rightarrow 3h$ | 6.3 | 15 | 0.9 | 1.3 | 0.17 |
| Total | $\varepsilon \times BR$ =10.6% | $\varepsilon \times BR$ =10.6% | 10.4 | 14.9 | 0.75 |

Table 3.3: Expected number of signal and background events in 5 years obtained in the search of $\nu_\mu \rightarrow \nu_e$ for 3 values of $\Theta_{13}$ and $\Delta m^2_{23} = 2.5 \times 10^{-3} eV^2$ and $\Theta_{23} = 45^0$. The numbers have been computed using the nominal design flux (numbers in parenthesis) and a flux increased by %50 corresponding $3.38 \times 10^{20} p.o.t.$ .

| $\Theta_{13}$ | signal $\nu_\mu \rightarrow \nu_e$ | $\nu_e CC$ | $\nu_\mu \rightarrow \nu_\tau$ $\tau \rightarrow e$ | $\nu_\mu NC$ | $\nu_\mu CC$ |
|---|---|---|---|---|---|
| $9^0$ | 13.9(9.3) | 27(18) | 6.7(4.5) | 7.8(5.2)) | 1.5(1.0) |
| $7^0$ | 8.7(5.8) | 27(18) | 6.9(4.6) | 7.8(5.2) | 1.5(1.0) |
| $5^0$ | 1.8(1.2) | 27(18) | 7.0(4.7) | 7.8(5.2) | 1.5(1.0) |

### 3.4.2 Recent status and the first events in the OPERA detector

The OPERA detector is still being installed and is about to come to the end. All electronics have fully been instrumented and tested. The ECC brick filling is in progress and about 142000 ECC bricks have already been inserted (90 % of target). In 2006 [62], the physics run started and it lasted 2 days due to a leak in the water cooling circuit of the reflector. During the physics run, in total, about $8.5 \times 10^{17}$ protons were delivered to the target. The average beam intensity was at the order of $\sim 1.4 \times 10^{13}$ on target (p.o.t.) per extraction at 400 GeV/c. The maximum beam intensity reached in 2006 was $1.75 \times 10^{13}$ p.o.t. per

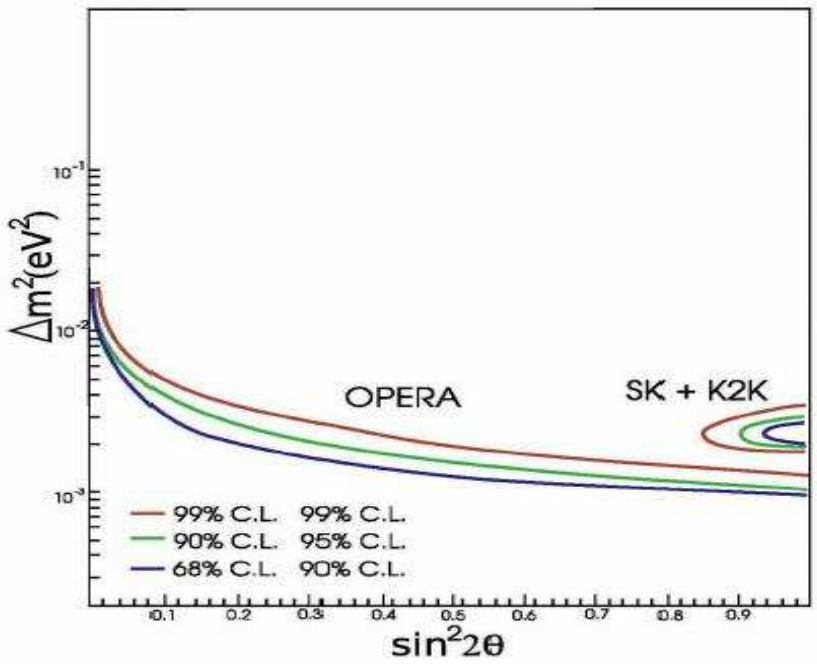


Figure 3.13: The sensitivity of the OPERA experiment to $\nu_\mu \rightarrow \nu_\tau$ oscillation.

extraction. The OPERA detector observed 319 beam events consistent with 300 events expected from the beam intensity. Physics run in 2007 started at 24th September and finished 20th October due to failure of the electronic controls of the ventilation system. The integrated time was about 5 days. The CNGS worked at %70 of the nominal power ($1.58 \times 10^{17 p.o.t/day}$) for a total number of p.o.t of $8.24 \times 10^{17}$ within these 5 days. In this run, 38 neutrino interactions in the brick were registered. These events were composed of 29 (CC) neutrino interactions and 9 (NC) neutrino interactions. A side view of the $\nu_\mu$ (CC) interaction in the electronic detector can be seen in Figure (3.14). A view of located $\nu_\mu$CC interaction with charm inside ECC is shown in Figure (3.15) (Figure (3.16)). The charm event reconstructed in emulsion film is shown in Figure (3.16).

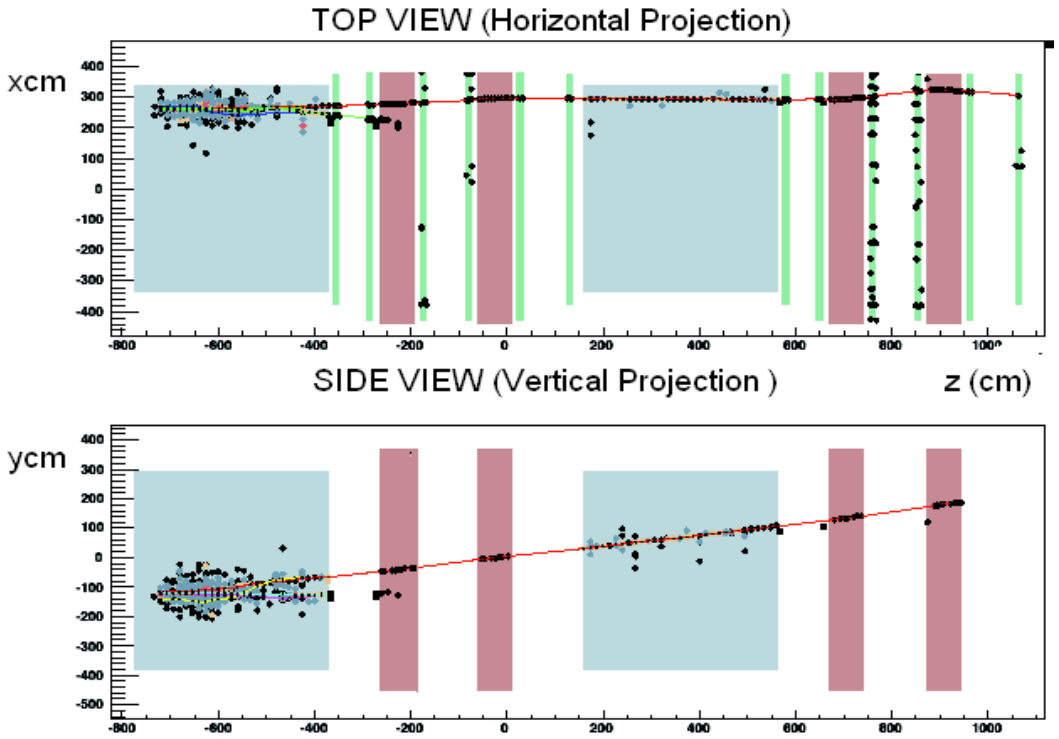


Figure 3.14: The illustration of the $\nu_\mu$ (CC) interaction in the electronic detectors.

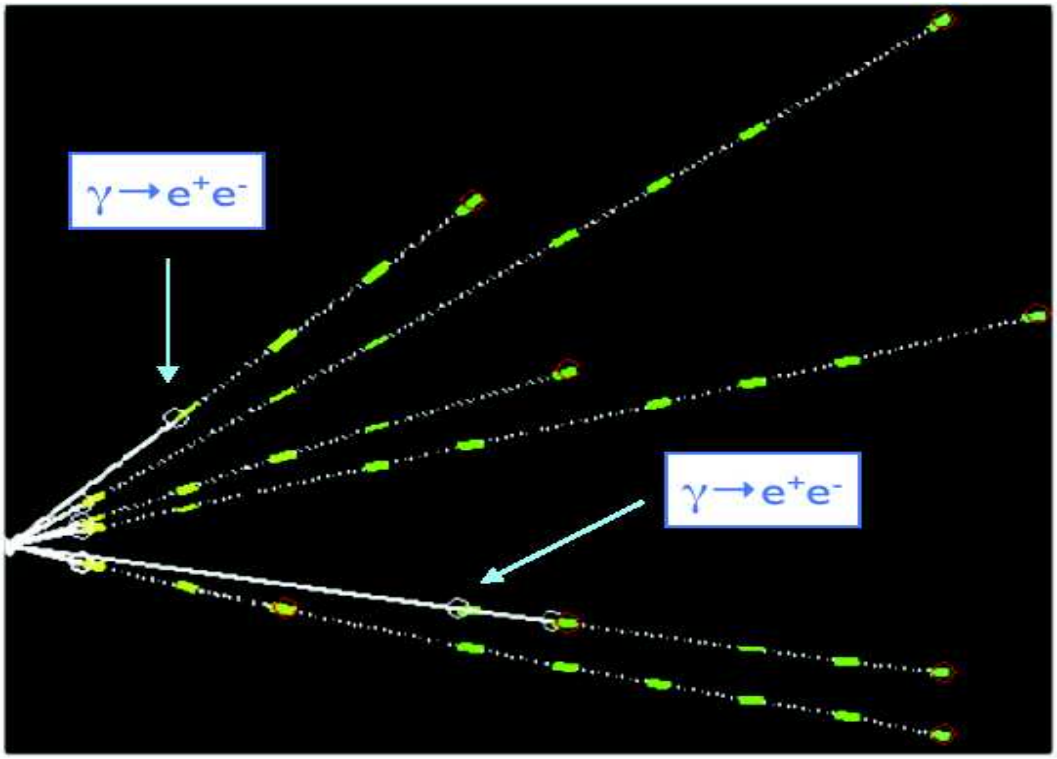


Figure 3.15: The side view of the reconstructed $\nu_\mu$CC interaction in the ECC brick.

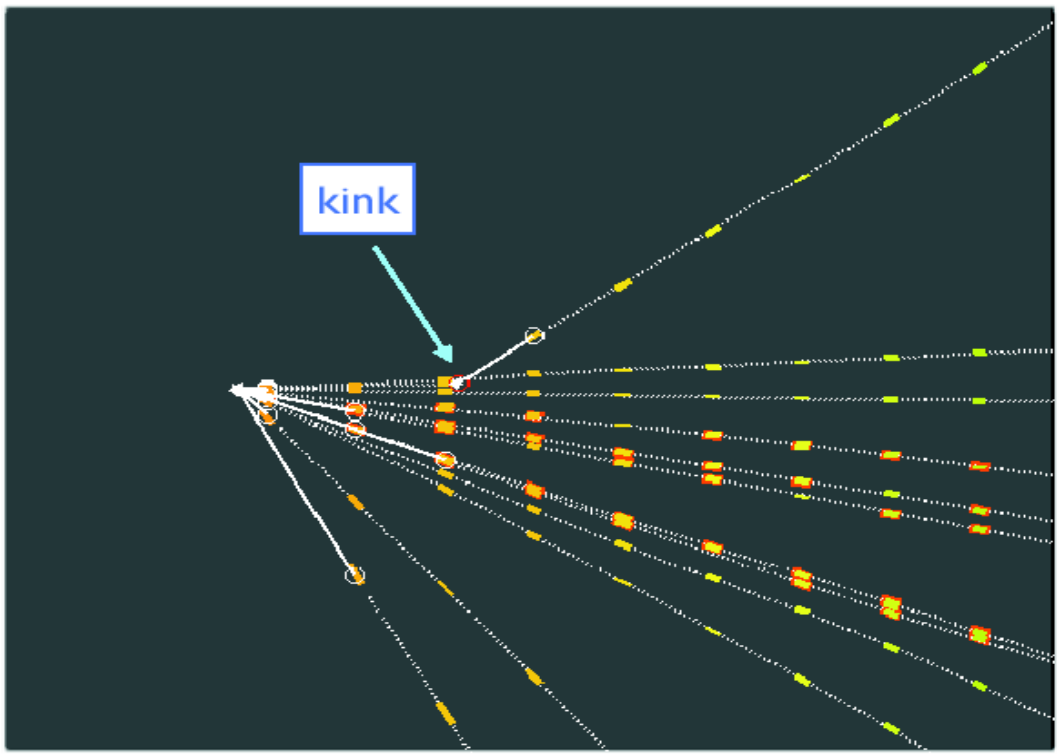


Figure 3.16: The side view of the reconstructed $\nu_\mu$CC interaction with a charm decay in the ECC brick.

# CHAPTER 4

# EMULSION SCANNING SYSTEM

The emulsion detectors utilized in long period experiments require very fast computer-controlled scanning systems because they are exposed to a great number of particles waiting for the reconstruction in a reasonable time frame. The automatic scanning system is composed of a microscope with motorized stages (X,Y and focuser), a microscope optical system, a CCD camera and controlling computer with a grabber-processor board and a motor control board [64]. The scanning of the nuclear emulsions is performed by the microscope whose vertical resolution is a few microns. By moving up and down the objective focal plane, the emulsion's separated frames are scanned one by one and the images processed are directed to the vision processor board, and then these images are reconstructed as a 3D structure of the particle tracks. Historically, the first automatic microscope system was developed by the Nagoya University in Japan as TS (Track Selector)system [65]. The TS and its renewed versions NTS (New Track Selector) and UTS (Ultra Track Selector) [66] was successfully used in CHORUS and DONUT experiments. The last version of the system is called Super UTS. Beside Japan Group, the European Group consisting of several laboratories developed the European Scanning System (ESS) to scan the OPERA emulsion films.

## 4.1 The European Scanning System

The segments of the ESS can be classified as: a rigid table, a granite arm, a motor driven scanning stage for both horizontal (XY) motion and vertical (Z) motion, an optical system with a digital camera, a vision processor board in the host PC and an illuminating system under the scanning table. The emulsion plates should be flat while scanning them, and therefore the emulsions are fixed onto a glass plate by the vacuum system placed on the corners of the glass plate.

### 4.1.1 The Mechanics

The Micos Company has provided the mechanics of the ESS in conformity with the OPERA experiment. The mechanics, the scanning table and the vertical stage, equipped with stepping motors were produced by Oriental Motor, and their controls are provided by the FlexMotion board of National Instruments hosted in the PC. The scanning table (X and Y movements) which is the model MS-8 has a range of 20.5 cm in XY directions and it has also 0.1 micron resolution optical encoder on both axis.

The horizontal motion speed is of great importance to acquire the needed performances of the system. The parameters such as the maximum speed, velocity, acceleration and deceleration profile, motor micro-steps have been set to minimize the time required to change field of view. The system displacement of the X direction and the Y direction is 350 $\mu m$ while the measurement occurs.

The vertical Z stage which is the Micos LS-100 model has been equipped with an integrated linear encoder 0.05 $\mu m$ resolution. During data acqusition, the vertical stage moves at a constant speed, in this case the constant velocity provides to have equally spaced emulsion images. It is tuned as depending on the emulsion thickness, on the dimension of the objective and on the glass plate. The European Scanning System at LNGS is shown in Figure (4.1)

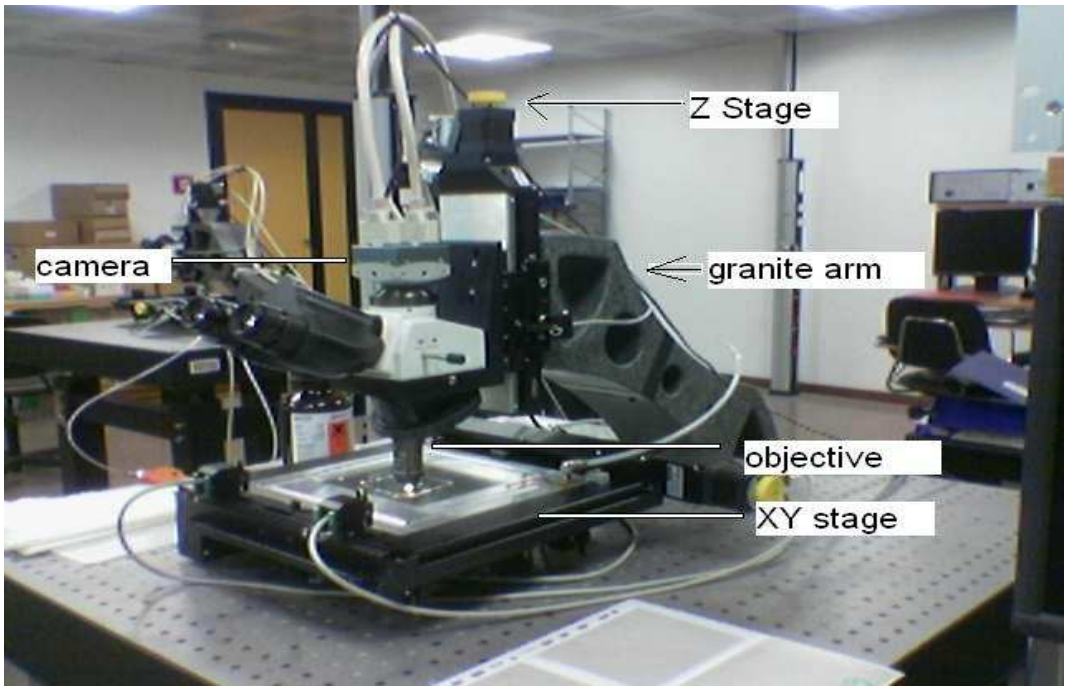


Figure 4.1: The European Scanning System (ESS) at LNGS scanning laboratory

### 4.1.2 Optics

The optical system consisting of objective and lens tube must provide high quality and resolution in order to scan sub-micron particle tracks. The objective is produced so that light emerging from the rear aperture is focused to infinity. A second tube lens hosted in the trinocular forms the image at its focal plane.

Emulsion films produced as layers on both sides of a 210 $\mu m$ thick transparent plastic base should be scanned by the objective providing two parameters. One of them is Working Distance (WD) larger than 300 $\mu m$ and the other is the Numerical Aperture (NA) larger than 800 $\mu m$ in order to acquire sub-micron

resolution. The oil-immersion is used to provide optically homogeneous medium between focal plane and objective. The immersion oils have a refractive index of 1.51, similar to the emulsion (1.51) and plastic base (1.48) refractive indices.

### 4.1.3 The Camera and the Vision Processor

The camera chosen in ESS is the Mikrotron MC1310 having a high-speed megapixel CMOS camera with Full Camera Link interface. The sensor delivers 10-bit monochrome 1280×1024 images at over 376 frames per second at full resolution. The European Scanning System reaches the scanning speed of $20cm^2/hr$.

The images inside nuclear emulsions are collected in a 256 gray level and these images are transferred to the frame grabber hosted in the PC. The frame grabber and the image processor are localized in the same the Matrox Odyssey Xpro board. It is designed for onboard image processing at high speed. Host PC is dual pentium workstation [67]. Each field of view is acquired in 40 ms.

### 4.1.4 The Light System

The light system located under the scanning table has been developed in cooperation with Nikon-Italy. The light before reaching the microscope base follows these ways: a collector lens, a glass diffuser and lastly it is focused on the aperture diaphragm of the sub-stage condenser. The field diaphragm is used because the emulsion can be illuminated or heated outside the field of view. The numerical aperture of the condenser has to match that of the objective in order to obtain a wide illumination cone and a high optical resolution. A glass diffuser and green filter provide a uniform illumination and a high optical resolution.

## 4.2 The Online Data Acqusition

The images on the emulsion plates are obtained by the ESS and the online DAQ provide micro-track reconstruction before off-line software for the track reconstruction. The online DAQ has been written in C++ language. The configuration and settings of the objects are controlled by a window panel including the modules of the scanning system and their functions. The modules of the scanning system and their functions are summarized in table(4.1).

Table 4.1: The modules of the scanning system and their functions.

| Modules | The Functions of the Modules |
|---|---|
| Objective | stores the information related to the used objective and performs the pixel to micron conversion |
| Odyssey2 | pilots the Odyssey board |
| FlexStage4 | is interfaced to the stage controllers and sets the motion |
| SmartTracker7 | performs the track pattern recognition, recognizing sequences of geometrically aligned clusters. |
| SmartFitter | performs the tracks fit. |
| DataIO | handles the Input/Output of data. |
| SheetMap2 | transforms coordinates and vectors from the current stage reference frame to the emulsion local reference system defined by a grid of fiducial marks printed on the emulsions. |
| VertigoScan5 | is the steering module, which uses all the other objects to control the scanning and its parameters |

The data taken is stored in Oracle Data Base and the images are formed as a

set of raw binary data. The images are collected at different gray levels changing from 0 to 256. The first level, 0, stands for black and the last one, 256th level, corresponds to white. These are sent to the Matrox board in order to search clusters. These clusters can be grains or fog. The image processing is provided by several steps, the first step is the flat field subtraction. The clusters of this step is useless and have to be removed because it leads to the reconstruction of vertical fake tracks. The aim of the following step, called as image filtering, is to enhance the contrast of dark spots on the lighter background. The filtering is processed by applying a convolution filter. Another step is the equalization procedure organizing the images as a homogeneous distribution of clusters inside the grabbed frames. The other step is the clusterization of the black spots. In this step, the black sequences inside each row are merged into a cluster, also these clusters are connected to each other. As a result, after all steps discussed above, position, area and shape of the clusters are localized as an information and stored as a output data.

### 4.2.1 Micro-track Reconstruction

The first step before the track reconstruction is the micro-track reconstruction in online DAQ procedure. The micro-tracks are reconstructed from the emulsion sides. The track recognition and the track fitting algorithms are used in order to obtain the reconstruction efficiently. The usage of the first algorithm is necessary for recognizing an array of grains as a track with the help of the geometrical alignments. The other algorithm including a linear fit provides to fit the position of the clusters and evaluation of the track slopes. The recognition algorithm starts with the search for a track start-up on the trigger layer. The field of view is divided into cells with 25 micron. The search of the start-up is processed inside the same cells. The trigger is the definition of the sequence of layers formed by two distant layers. A clusters found in a cell is linked with a line with the other

aligned cluster inside another cell on the different layer. The production of the trigger depends on finding at least one another cluster in a different cell. After finding the start-up. The algorithm follows the another tracks at the other layers. As soon as all clusters are found, a bidimensional linear fit is processed and also clusters are removed from the tracks. The tracks are stored in the output file as depending on the number of grains.

## 4.3 Track Reconstruction in ECC

With the help of the online DAQ procedure, micro-tracks are found and reconstructed. Track reconstruction process including base-tracks and volume tracks continue as linking of the micro-tracks, plate by plate alignment and volume track reconstruction. A schematic view of the micro-track and base-track reconstruction are seen in Figure (4.2). The FEDRA programme [68] is used for the off-line base-track and volume track reconstruction. The FEDRA, an object-oriented tool, has been written in C++ language developed in Root Framework.

### 4.3.1 Linking of the Micro-tracks : Base-Track Reconstruction

As seen in Figure (4.3), the base-track is reconstructed by connecting a pair of micro-tracks across the plastic base and by searching for consistency within given position and slope tolerances. The calculation of $\mathcal{X}^2$ for a couple of micro-tracks satisfying position and angular cuts can be given as follows:

$$\mathcal{X}^2 = \frac{1}{4}[\frac{(\theta_{zt} - \theta_{xB})^2}{\sigma_x^2} + \frac{(\theta_{xb} - \theta_{xB})^2}{\sigma_x^2} + \frac{(\theta_{yt} - \theta_{yB})^2}{\sigma_y^2} + \frac{(\theta_{yb} - \theta_{yB})^2}{\sigma_y^2}], \qquad (4.1)$$

where $\theta_{zt(b)}$ and $\theta_{yt(b)}$ are the longitudinal and transverse projections of the top (t) and bottom (b) micro-track slopes in the z-x plane and z-y plane, $\theta_{zB}$ and $\theta_{yB}$ are the same projections for the base-tracks (B) and $\sigma_x$ and $\sigma_y$ are the micro-tracks angular resolutions.

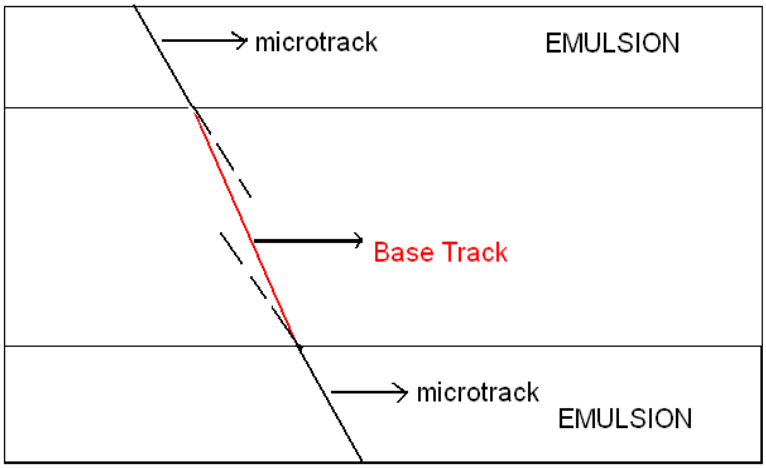


Figure 4.2: A schematic view of micro-track and base-track in emulsion.

### 4.3.2 Plate to Plate Alignment

The emulsion plates are separated in several cells while scanning the plates and for each cell, a pattern recognition between base-tracks of two consecutive emulsion films are performed in order to realize plate to plate alignment. Generally, 1-2 cosmic ray $muons/mm^2$are enough for an accurate plate to plate alignment. One of the patterns is selected as a reference point by the algorithm and the other patterns are shifted till the maximum number of track coincidences is obtained. The description of the alignment pattern is provided by the affine transformation:

$$\begin{pmatrix} x' \\ y' \end{pmatrix} = \begin{pmatrix} a_{11} & a_{22} \\ a_{21} & a_{22} \end{pmatrix} \begin{pmatrix} x \\ y \end{pmatrix} + \begin{pmatrix} b_1 \\ b_2 \end{pmatrix}. \tag{4.2}$$

### 4.3.3 Volume Track Reconstruction

The last step of tracking is volume track reconstruction. The process of the plate to plate alignment is followed by connecting base-tracks in order to reconstruct volume track inside ECC. Firstly, the base-tracks are connected to each other with the related algorithms. Secondly, these base-track couples form long chains of segments. Lastly, the track propagation is found by taking into account the possibility of loosing base-track segments on one or more plates.

# CHAPTER 5

# TEST EXPERIMENT FOR ELECTRON IDENTIFICATION

## 5.1 CERN SPS-H4 Beam Line

The H4 beam, a part of the SPS North Area (EHN1), is a secondary particle beam that provides hadrons, electrons or muons of energies between 10 and 360 GeV/c, as well as 400 GeV/c (primary) protons. A 400 (450) GeV/c primary proton beam is extracted from the SPS towards the North Areas, split into three beams, one of which is directed onto the T2 primary target. The typical intensities of this primary beam are a few $10^{12}$ protons per burst. The H4 and H2 beams to EHN1 are derived from the T2 target and thanks to the T2 wobbling station. The multi-purpose T2 wobbling station is shown in Figure (5.1). The control of H4 beam line is done with the graphical user interface CESAR. Steering and Focussing of the beam are provided by the BENDs, QUADs and TRIMs. Steering of a beam is done by BENDing magnets (dipoles). Quadrupoles are like lenses in conventional optics, they are used to (de-)focus the beam and thus change the spot size of the beam. The spot size of the beam is controlled by the last QUADs in front of each set-up.

Trim magnet are correction the dipoles used for fine steering of the beam. The beam intensity is normally controlled by three collimators, namely: C1 (filter

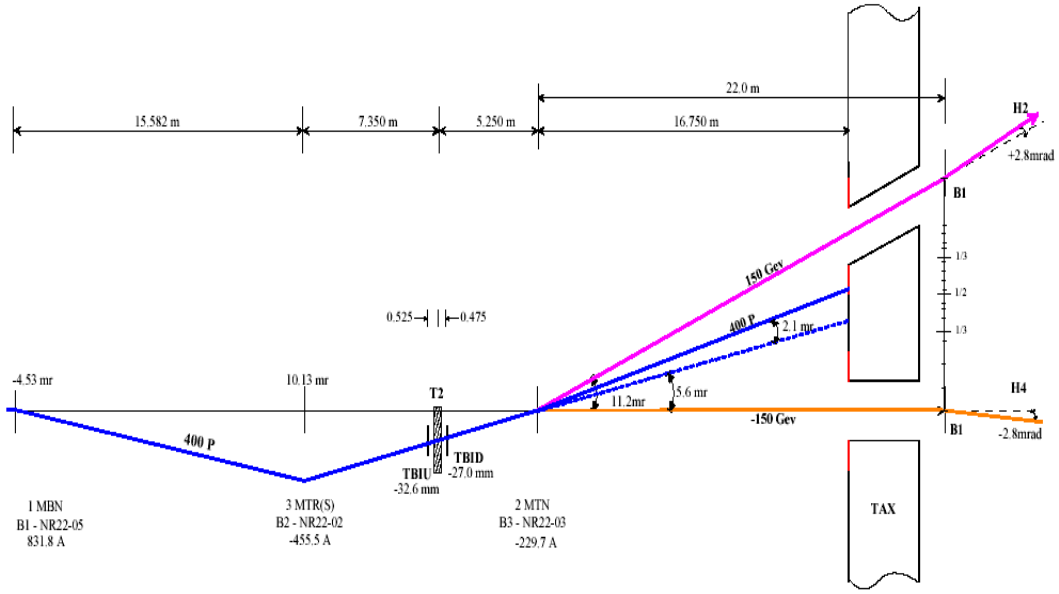


Figure 5.1: This is the "multi-purpose" T2 wobbling setting.

mode) or C2 (HR and HT mode) Horizantal Acceptance, C3 Momentum defining (vertical), C6 Vertical Acceptance.

### 5.1.1 The Experimental Set-Up

The OPERA bricks were used to study the behavior of electron showers in ECC. Test exposure was performed in July 2007 at CERN SPS-H4 Beam Line, in a collaboration with Utsonomiya and Nagoya University. The ECC bricks prepared in BAM facility in LNGS were transported from LNGS to CERN. The ECC bricks were exposed to electron and muon beams at different angles. In order to have exposure at different angles, the ECC bricks were placed on a

target mover in front of the H4 Beam line. The experimental area at CERN is shown in Figure (5.2).

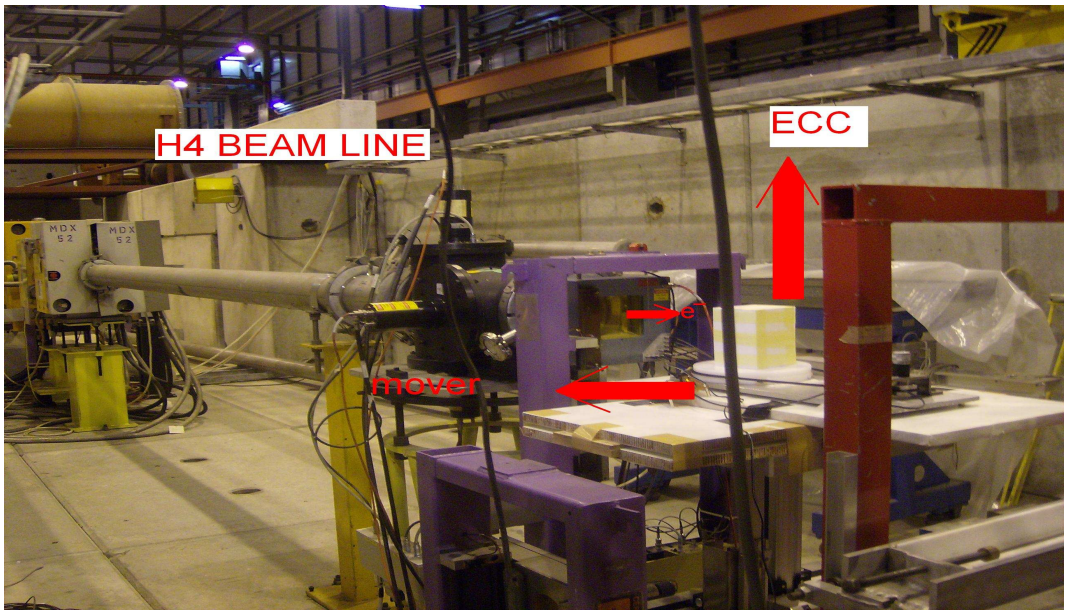


Figure 5.2: The H4 Beam Line.

The motion of the ECC brick in up-down and left-right direction were controlled by the remote control. The control of electron and muon beam was also being monitored in the barrack by the graphical user interface programme CESAR. The z axis is defined as the perpendicular direction with respect to the ECC surface. The ECC surface was oriented in such a way that the electron beam direction with respect to the z axis was shifted by 50 mrad. The angles at which electron beam were exposed are (0, -50 mrad) and (0, 50 mrad) for 50 GeV and 20 GeV beams, respectively. On the other hand, the z axis was also shifted

Table 5.1: The angle and energy conditions of the beam.

| Particle | Energy (GeV) | Counts Accumulation | Angle (mrad) |
|---|---|---|---|
| Electron | 20 | 88 | 50 |
| Electron | 50 | 103 | -50 |
| Muon | 150 | $3 \times 10^3$ | -300,-250,-200,-150,-100 |
| Muon | 150 | $3 \times 10^3$ | 0,300,250,200,150,100 |

for the 150 GeV muon beams. The spot sizes of the electron and muon beams were $3cm \times 3cm$ and $8cm \times 8cm$, respectively. The muon ($\mu^+$) beam exposed for plate to plate alignment were directed at different angles from -300mrad to +300mrad with +50 mrad intervals, except for -50mrad and 50mrad angles. The electron beam exposure was performed to obtain 88 and 103 counts accumulation inside the ECC for 20 GeV and 50 GeV electron beam, respectively. The muon beam exposure was organized as $3 \times 10^3$ counts accumulation into the ECC brick for different angles. A list of the angle and energy conditions can be seen in Table (5.1).

## 5.2 Data Acqusition

All emulsion plates were developed and scanned in LNGS. Due to the time limitation, only 39 (out of 57) emulsion plates were scanned. The scanning area was set to $3cm \times 5cm$ with respect to center of the plate. The schematic view of the scanned area is shown in Figure (5.3).

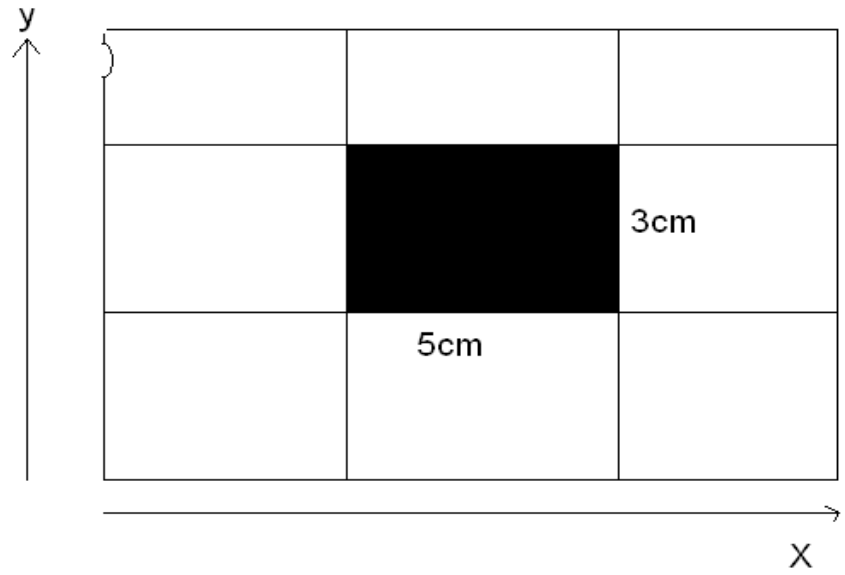


Figure 5.3: A schematic view of scanned area.

# CHAPTER 6

# ELECTRON SHOWER ANALYSIS

As explained in previous sections, OPERA project is an appearance experiment and is searching for $\nu_\mu \rightarrow \nu_\tau$ oscillations in the parameter region indicated by atmospheric neutrino experiments. The signal of $\nu_\mu \rightarrow \nu_\tau$ oscillation is identified by the detection of the tau lepton's decay topology and one of the decay modes is $(\tau^- \rightarrow e^- \nu_\mu \overline{\nu_e})$. Beside $\nu_\mu \rightarrow \nu_\tau$ oscillation, the OPERA detector is also capable of searching for $\nu_\mu \rightarrow \nu_e$ oscillations by detecting $\nu_e$CC interactions. Both in $\nu_e$CC interactions and in $\tau$ decay mode into electron, the identification of electron inside ECC will be a main subject of the OPERA experiment. Electron tracks generate their own topology having the shape of the electron cascades. Electron tracks in the ECC brick should be reconstructed properly in order to identify electron.

In the next section, the behavior of the heavy particles passing through a material will be explained. Their energy loss mechanism for charged particles inside material will be mentioned. The results on electron shower reconstruction will be presented in the following section.

## 6.1 Passage of Particles Through Matter

The detection of a particle depends on interaction in the material of the detector. The most important interaction for particle detection is the electromagnetic interaction. Relativistic charged particles heavier than electron lose energy by

excitation and ionization of atomic electrons. The Bethe-Bloch equation gives

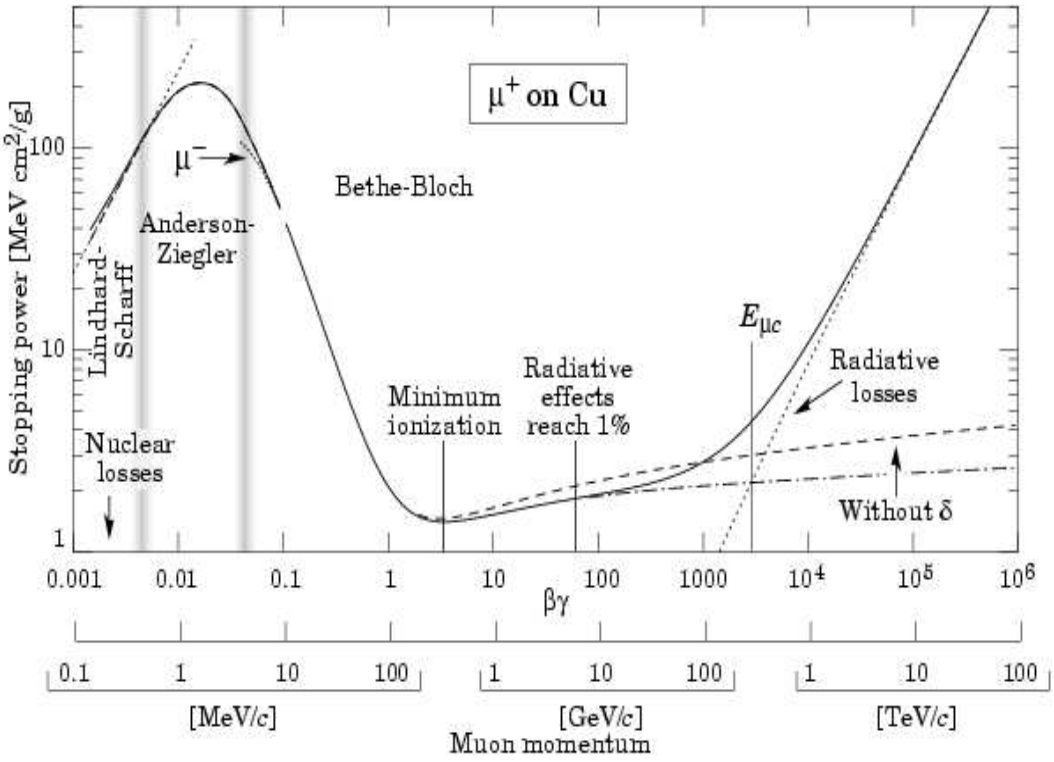


Figure 6.1: Stopping power ($=< -\frac{dE}{dx} >$) for positive muons in copper as a function of $\beta\gamma = \frac{p}{Mc}$ over nine orders of magnitude in momentum (12 orders of magnitude in kinetic energy). Solid curves indicate the total stopping power.

the mean rate of energy loss (or stoping power) and is given by [69]

$$-\frac{dE}{dx} = Kz^2\frac{Z}{A}\frac{1}{\beta}[\frac{1}{2}ln\frac{2m_ec^2\beta^2\gamma^2T_{max}}{I^2} - \beta^2 - \frac{\gamma}{2}], \tag{6.1}$$

where $T_{max}$ stands for the maximum kinetic energy which can be imparted to a free electron in a single collision, z is the charge of the incident particle, Z and A are the atomic number and the atomic mass of the absorber, respectively. I is

the mean excitation energy measured in eV, with $K/A = 4\pi N_A r_e^2 m_e c^2$ measured in $MeV g^{-1} cm^2$ and A in $gmol^{-1}$.

The function, as computed for muons on copper, is shown by the solid curve in Figure (6.1). Particles passing through any material lose their energies in different ways. More comprehensive discussion of the energy loss mechanisms can be found in [70].

## 6.2 Electromagnetic Shower Formation inside the Matter

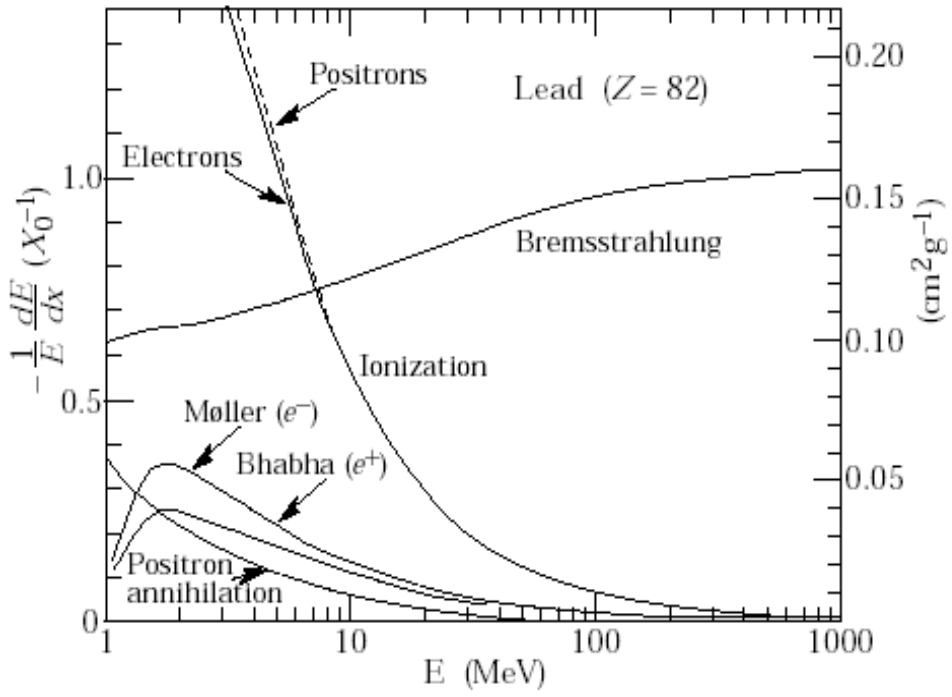


Figure 6.2: Fractional energy loss per radiation length in lead as a function of electron or positron energy.

The interaction of electrons and photons with matter have various energy loss mechanisms. Electrons whose energies are higher than 100 MeV lose energy almost entirely through bremsstrahlung mechanism. This mechanism is a dominant energy loss mechanism for high energy electrons and it causes electromagnetic radiation. The figure (6.2) shows energy loss of electrons in lead. Photons with energy above 100 MeV undergo pair production by producing electron and positron. The intense electric field near the nucleus can cause the photon to decay into an electron and a positron. Pair production may also occur near an atomic electron. In this case, a photon or an electron inside matter is able to produce electromagnetic shower. The simplified development of an electromagnetic shower is shown in Figure (6.3). As soon as energy of the particle falls below 100 MeV, the shower production stops. The shower develops in the forward direction and it has the longitudinal and transverse developments. The longitudinal development is dominated by the photons. The critical energy $E_c$ is defined as the energy at which the loss by radiation is equal to the loss by ionization. The equation of the critical energy was theorized by Berger and Seltzer [71] as a function of the atomic number:

$$E_c = \frac{800}{Z + 1.2}(MeV). \tag{6.2}$$

The unit of distance traversed is typically measured in radiation lengths, the radiation length $X_0$ is also defined as the distance over which the energy of the electron is reduced by a factor *1/e* by bremsstrahlung only. It is parametrized in terms of Atomic number (Z) and Atomic weight(A) as

$$X_0 = 716.4 \frac{A}{[Z(Z+1)ln(\frac{287}{\sqrt{Z}})]} g.cm^{-2}. \tag{6.3}$$

The mean longitudinal shower development is given by [72]

$$\frac{dE}{dt} = E_0 b \frac{(bt)^{a-1} e^{-bt}}{\Gamma(a)}, \tag{6.4}$$

where $t = \frac{x}{X_0}$ is the depth in radiation length, $E_0$ is the incident energy, $a$ an $b$ are parameters depending on the incident particle, $e^{\pm}$ or $\gamma$. The transverse dimension is measured in terms of the Moliere radius [73] defined by

$$R_M = X_0 \frac{E_s}{E_c}, \tag{6.5}$$

where $E_s \simeq 21MeV$. A simple model giving the correct qualitative description of the longitudinal development of a shower was given by Heitler [74, 75]. The assumptions of the model are a) Each electron with $E > E_c$ travels 1 radiation length and then gives up half its energy to a bremssrahlung photon. b) Each photon with $E > E_c$ travels a radiation length and then undergoes pair production with each created particle receiving half of the energy of the photon. c)Electrons with $E < E_c$ cease to radiate and lose their remaining energy to collisions. d) Neglect ionization losses for $E > E_c$. This model says that after the first radiation length, energy of any photon or electron falls down to $E_0/2$. Electron emits a second photon in the second radiation length, while the first photon makes pair production by decaying into an electron-positron pair. Thereby, at the end of the two radiation lengths, there will be one photon, one positron and two electrons, each with energy $E_0/4$. The model of Heitler gives a number of properties of electromagnetic showers. The total number of particles inside the electron shower after $t$ radiation lengths is given by

$$N(t) = 2^t = e^{tln2}. \tag{6.6}$$

The average energy of a shower particle at the depth is

$$E(t) = E_0/2^t. \tag{6.7}$$

The shower has the maximum number of particles when $E(t) = E_c$. This happens at the depth

$$t_{max} = \frac{ln(E_0/E_C)}{ln2}. \tag{6.8}$$

The number of particles at the maximum depth is

$$N_{max} = e^{t_{max} ln2} = E_0/E_c. \tag{6.9}$$

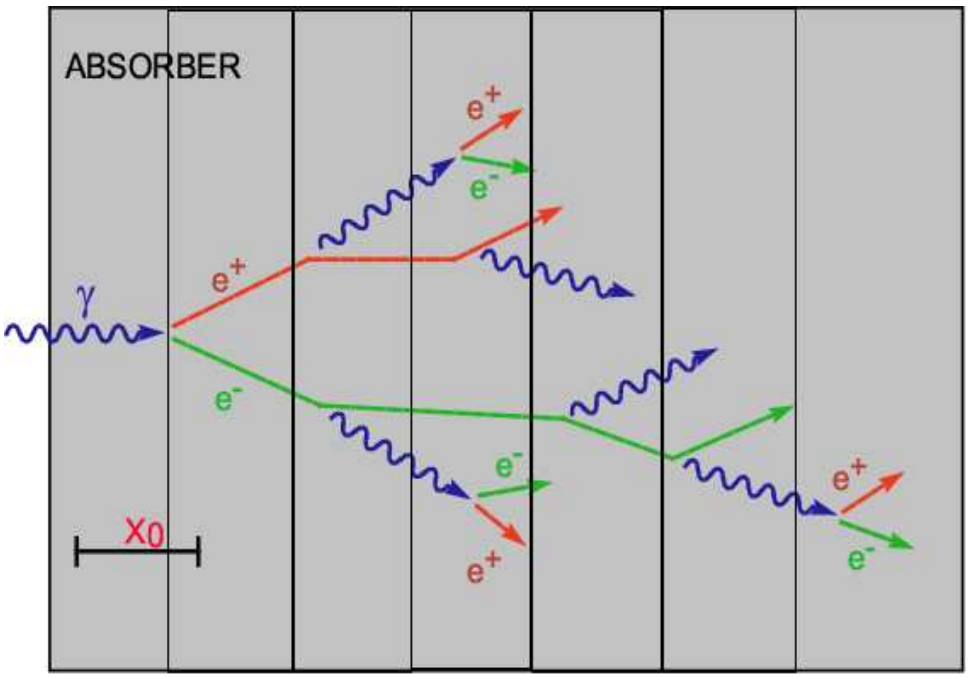


Figure 6.3: A simple model for the development of an electromagnetic shower. Solid lines indicate electron and positron and wavy lines indicate photons.

## 6.3 The Electromagnetic Shower Algorithm

In section (4.6), the FEDRA reconstruction code is described as a tool of track reconstruction and all reconstruction procedure related to micro-track, base-track, plate to plate alignment and volume-track reconstruction is clearly explained. The algorithm to reconstruct electron shower based on base-tracks inside a defined cone was described in the OPERA proposal [76]. An electron

or photon is enough to construct shower cascades inside the ECC brick. By the electromagnetic interaction inside the brick, a base-track called "selector" occurs in the most up-stream emulsion sheet. Shower algorithm starts the propagation from the "selector". The algorithm for the reconstruction of the shower continues as depending on an iterative procedure. Base-tracks matching the selector in the downstream films are connected to each other. This connection criteria depends on angular ($\delta\theta$) and position ($\delta r$) requirements. The angular displacement ($\delta\theta$) is described as the angle difference between the selector and the base-track candidate. The position displacement ($\delta r$) is the transverse distance between the selector and the candidate extrapolated back to the selector. As a result of this iterative procedure, a found base-track matching the selector is again called as the selector and the procedure continues. To take into consideration the shower reconstruction efficiency, the base-track candidate or the selector is allowed to be connected at maximum 3 emulsion plates, and then it is eliminated. There are some various background signals affecting the shower reconstruction , this background should be rejected by applying a fiducial volume cut around the shower axis. Because the electron shower cascades develop at the longitudinal and the transverse directions, base-tracks have to be inside a cone (with axis defined by the slope of the first base-track a part of the shower) with an opening angle of 20 mrad. The overlapping of the other close base-tracks coming from the different electron shower cascades can be rejected by keeping the radius of the cone stable after reaching 400 micron. As a result, the cone turns into a cylinder with a radius of 400 micron after 15 emulsion plates. In addition, in order to eliminate irrelevant background, the base-tracks selected as a track starting outside the fiducial volume is rejected. The purity of the shower algorithm can be calculated by searching showers at different angle spots which correspond to muon particles. By this method, we estimate background contamination. A schematic view of the cone for the electron shower reconstruction can be seen in Figure (6.4).

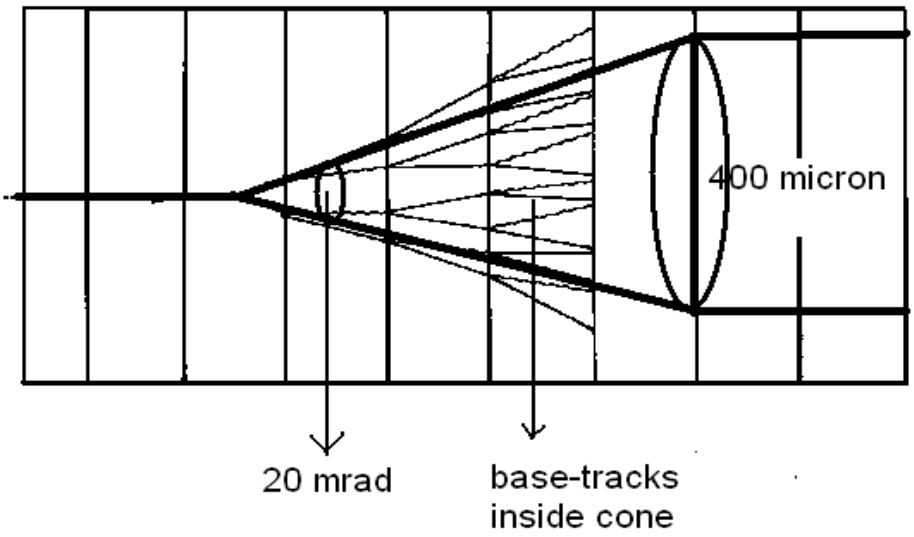


Figure 6.4: A schematic view of the cone used for the electron shower reconstruction.

## 6.4 Analysis and Results

In this study, an ECC brick was exposed to electron beam in order to study electron identification. The brick thickness in terms of radiation length is 10 Xo and thus an electron shower is well confined within a single brick. The ECC brick was exposed to electron and muon beam at different angles as given in Table (5.1), the aim of the muon exposure is to provide plate to plate alignment of emulsion plates within the ECC brick. We scanned 39 emulsion plates of the ECC brick as an area of 5cmx3cm as seen in Figure (5.4). But in this analysis, we have used the data of 29 plates. This data has been reconstructed by the

off-line track reconstruction software (FEDRA). The electron and muon tracks were collected as a set of raw data by the online data acquisition process and then it was converted into root files. The information the on-line DAQ procedure obtained was the detected micro-tracks plus some general information related to the acquisition process. As mentioned in section (4.6), after the morphological information of the clusters (position, area, ...) is processed, the process goes on using the information to recognize geometrical alignments between clusters of different layers in order to reconstruct micro-tracks. A base-track was built by connecting two micro-tracks that cross the plastic base , and volume-track was constructed from two or more base-tracks, each one was in a different emulsion plate. Thus, the trajectory of a particle transversing an ECC was reconstructed. Briefly, all these steps, obtaining clusters, micro-tracks, base-tracks and volume-tracks lead to reconstruction of electron shower. The algorithm explained in previous section was used for the electron shower reconstruction. The electron reconstruction is based on the angular distribution of base-tracks shown in Figure (6.5) and Figure (6.6). The angle of the selector track is taken to be (0, $20 \pm 10$ mrad) and (0, -48$\pm$12 mrad) for 20 GeV and 50 GeV electron beam, respectively.

Then by applying the shower algorithm we have found 30 electron showers (29 events are at 20 GeV and 1 event is at 50 GeV) in the brick. One of the reconstructed electron shower is shown in Figure (6.9) (Figure (6.10)) for 20 GeV (50 GeV) electron beam. The position of base-tracks in the shower is shown in Figure (6.7) and Figure (6.8).

The background contamination in the electron shower coming from close electron shower, cosmic rays and fogs were estimated by comparing base-tracks in 20 GeV electron shower cone with a randomly selected area having no electron shower profile but containing the base-tracks. The mean number of base-tracks in the randomly selected area is found to be $20 \pm 4$. The position distributions of base-tracks belonging to electron shower and background are shown in Figure

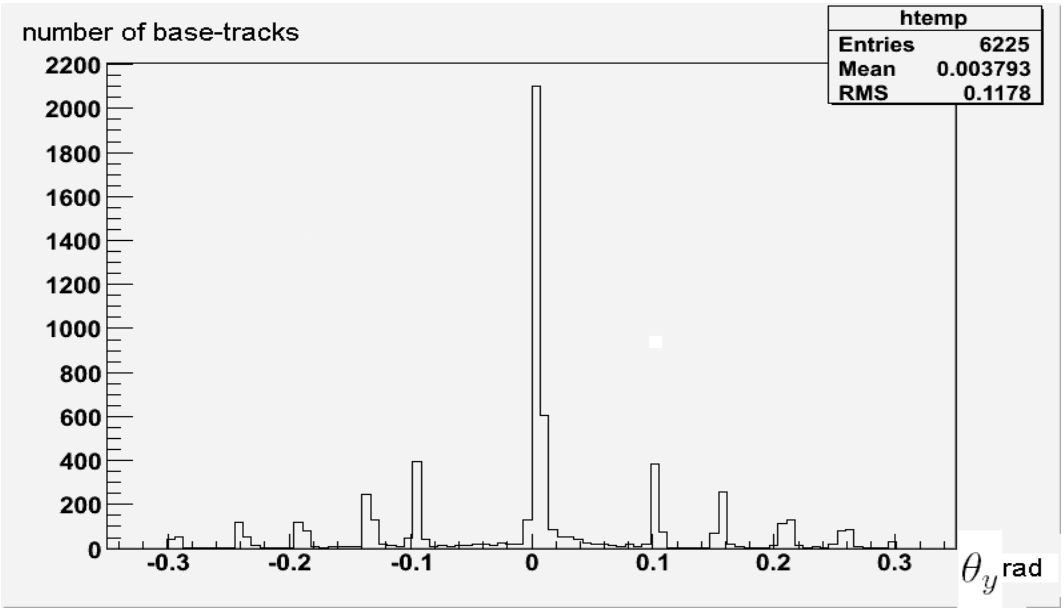


Figure 6.5: The angular distribution of the muon and electron base-tracks in $\Theta_y(radyan)$. The signal peaks of electron beam are lower than the signal peaks of the muon beam because the muon density is much more than electron density. The distribution changes from -0.3 (radyan) to 0.3 (radyan).

(6.11) and Figure (6.12).

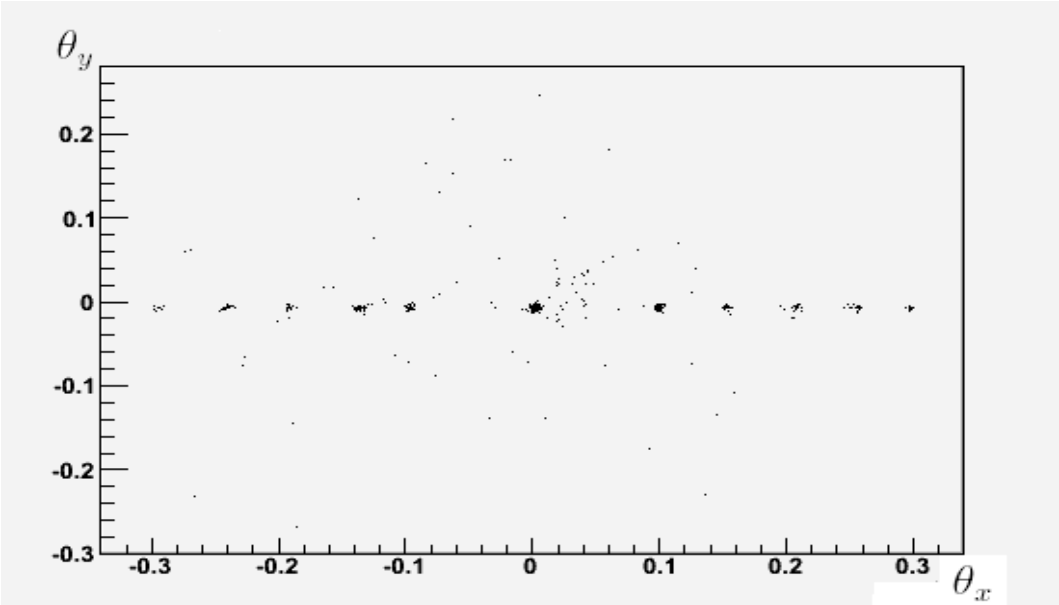


Figure 6.6: The angular distribution of the muon and electron base-tracks in $\Theta_y(radyan)$ and $\Theta_x(radyan)$. The distribution changes from -0.3 (radyan) to 0.3 (radyan).

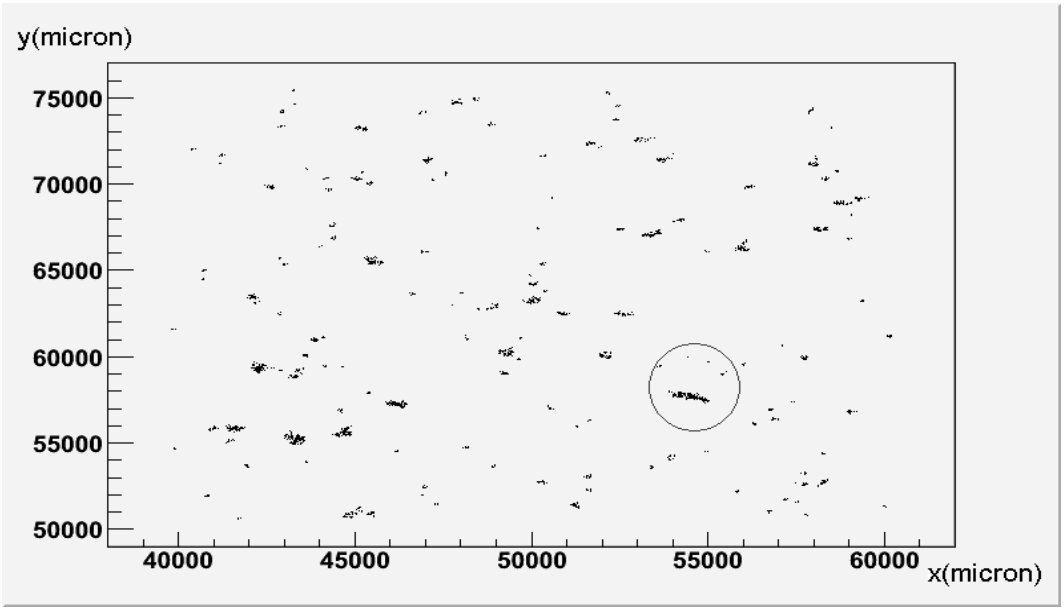


Figure 6.7: The illustration of the reconstructed 20 GeV electron shower base-tracks seen from up-stream face of the ECC. The enclosed area corresponds to the localized electron shower shown in Figure (6.9).

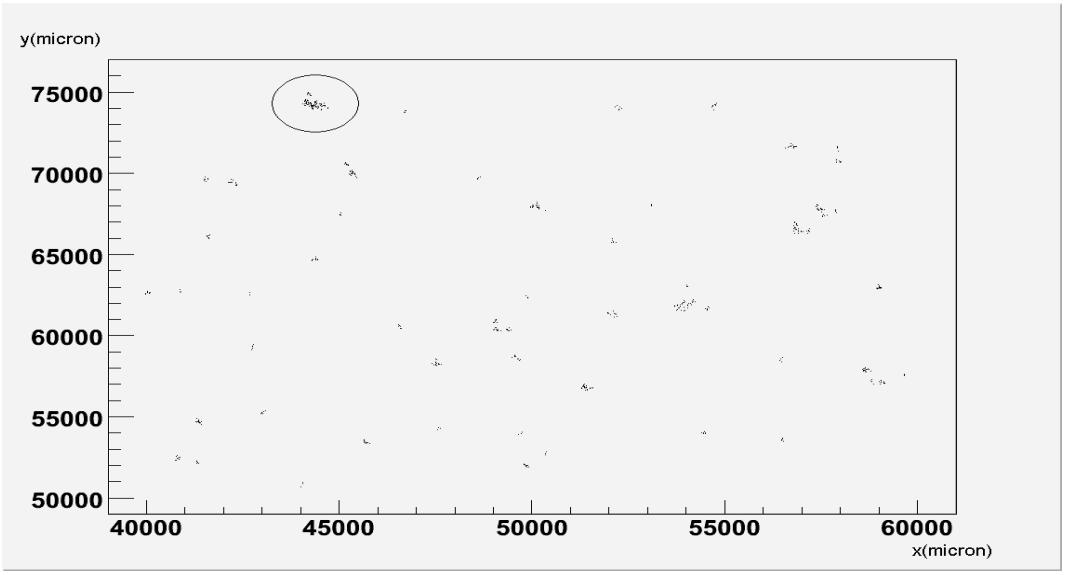


Figure 6.8: The illustration of the reconstructed 50 GeV electron shower base-tracks seen from up-stream face of the ECC. The enclosed area corresponds to the localized electron shower in Figure (6.10).

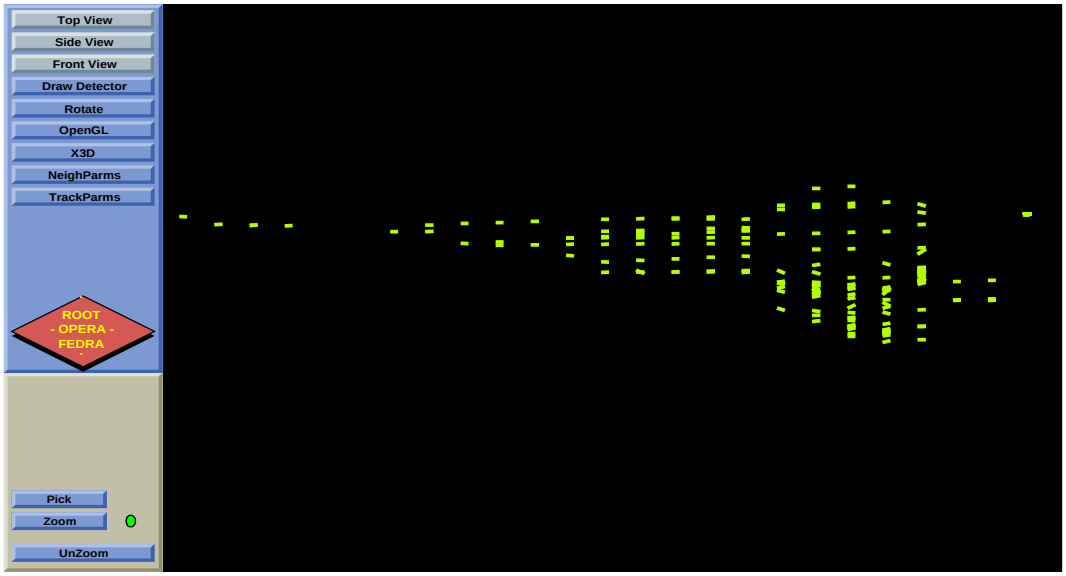


Figure 6.9: The illustration of a reconstructed electron shower generated by a 20 GeV electron interacting the ECC brick. Each segment corresponds to a base-track with respect to the reconstructed electromagnetic shower.

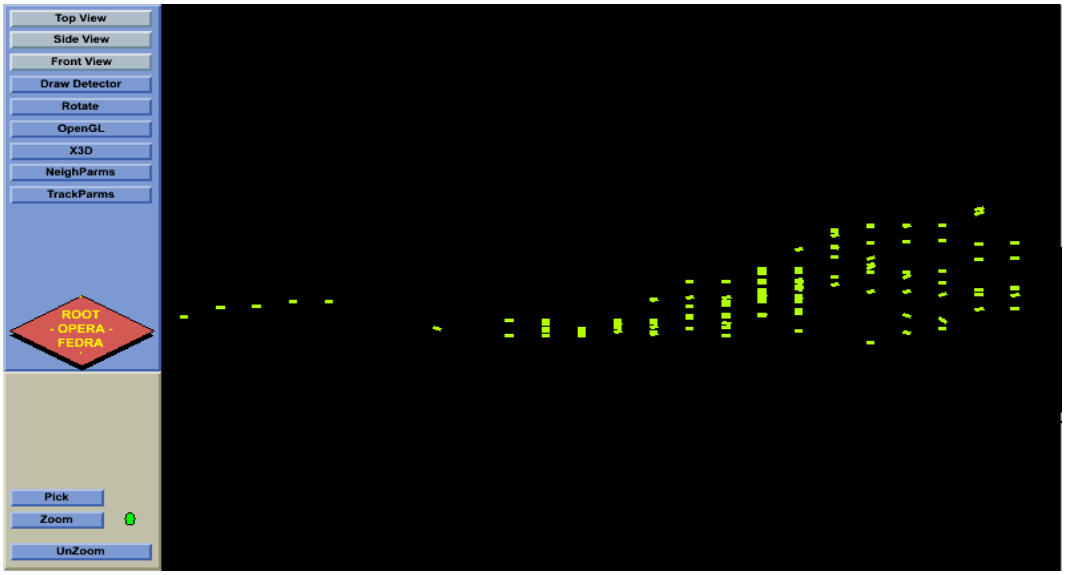


Figure 6.10: The demonstration of a reconstructed electron shower generated by a 50 GeV electron.

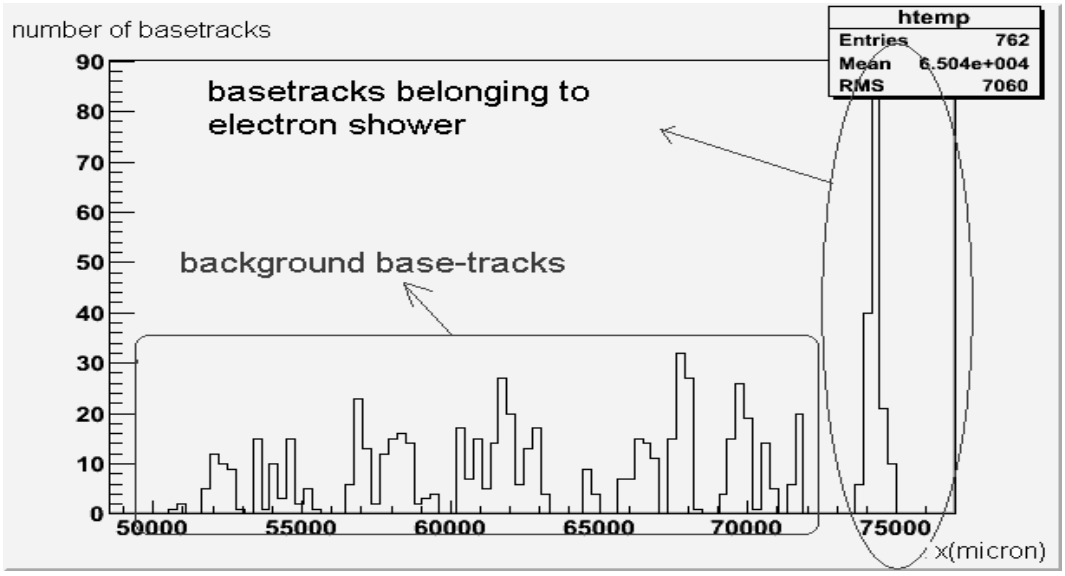


Figure 6.11: x position of base-tracks in the area of $2.5cm \times 2cm$ around 50 mrad spot.

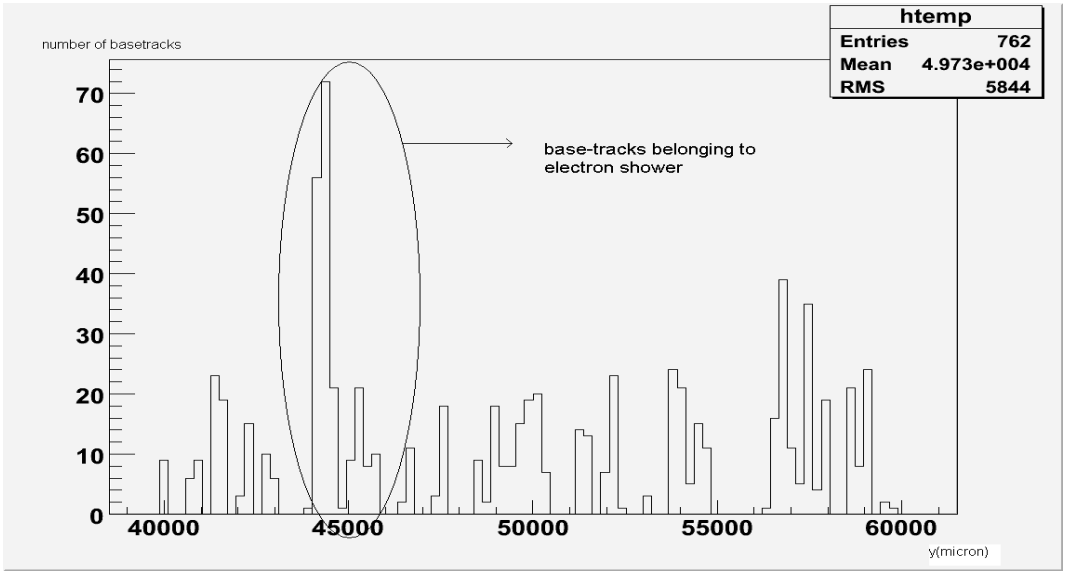


Figure 6.12: y position of base-tracks in the area of $2.5cm \times 2cm$ around 50 mrad spot.

# CHAPTER 7

# CONCLUSION

The detection of neutrino oscillations will open the gate of the new physics beyond the SM. The OPERA detector, located in LNGS laboratory, is designed to search for $\nu_\tau$ appearance in an almost pure $\nu_\mu$ beam. OPERA is a hybrid detector consisting of the ECC and some electronic detectors for a rough location of the events in the ECC brick and for full event reconstruction. The search is based on the observation of $\nu_\tau$CC interactions and subsequent decay of $\tau$-lepton into electron, muon and single charged hadron in the ECC brick. The neutrino beam (CNGS) with a baseline of 730 km is optimized for $\nu_\tau$ appearance. The total length of an ECC detector, about 10 $X_0$, allows an efficient electromagnetic shower analysis. An electron quickly develops an electromagnetic shower in lead, and then, the total number of tracks, as well as the different longitudinal and transverse profiles of the electron showers can be then used for particle identification. Having a good electron identification in the ECC brick OPERA can explore $\nu_\mu \rightarrow \nu_e$ appearance channel in addition to the dominant $\nu_\mu \rightarrow \nu_\tau$ channel. Therefore, electron identification is a very important issue in the experiment for signal extraction and background suppression. The main contribution of this thesis is to study electron identification algorithms for the reconstruction of neutrino interactions in the OPERA detector. An ECC brick was exposed to electron beam at CERN. The emulsion films were developed and scanned in LNGS. The FEDRA framework, an object-oriented tool, were used for the off-line base-track

and volume track reconstruction. In total, 30 electron showers were found: 1 event is at 50 GeV and 29 events are at 20 GeV. Background contamination due to shower overlap and passing through cosmic rays was estimated to be $20 \pm 4$.

# REFERENCES


[1] B. Pontecorvo, Zh. Exp. Fiz. 33 (1957) 549.

[2] Y.Fukuda, et al. (SuperKamiokande Coll.), *Phys.Rev.Lett.*, **81**, 1562(1998).

[3] Y.Fukuda, et al. (SuperKamiokande Coll.), *Phys.Lett.*, **B433**,9(1998); *Phys.Rev.Lett.*, **85**,399 (2000).

[4] M.Guler, et al.(OPERA Coll.), *Experimental Proposal*, CERN-SPSC-2000-28;M.Guler et al.(OPERA Coll.), *Status Report on the OPERA Experiment*, CERN-SPSC-2001-025.

[5] J.Chadwick, *Distribution in intensity in the magnetic spectrum of the $\beta$-rays of radium* ,Verh. Deutsch Phys. Ges. 16, 383 (1914).

[6] E.Rutherford, *Collisions of alpha particles with light atoms. IV. An anomalous effect in nitrogen*, Phil. Mag. 37, 581 (1919).

[7] J.Chadwick, *Possible existence of a neutron*,Nature 129, 312 (1932).

[8] F.Reines and C.L. Cowan, Phys. Rev. Lett. **92**,830 (1953).

[9] R.N.Mohapatra and P.B.Pal, *Massive Neutrinos in Physics and Astrophysics*, River Edge, N.J. World Scientific, 2004.

[10] G. Danby et al., *Observation of high-energy neutrino reactions and the existence of two kinds of neutrinos*,Phys. Rev. Lett. 9, 36 (1962).

[11] M. L. Perl et al., *Evidence for anomalous lepton production in $e^+e^-$ annihilation* ,Phys. Rev. Lett. 35, 1489 (1975).

[12] K. Kodama et al., DONUT Collaboration, *Observation of tau-neutrino interactions* ,Phys. Lett. B504, 218 (2001).

[13] S. L. Glashow, *Partial symmetries of weak interactions* , Nucl. Phys. 22, 579 (1961).

[14] S.Weinberg , *A model of leptons* , Phys. Rev. Lett. 19, 1264 (1967).

[15] Proceedings of the Eighth Nobel Symposium, edited by N. Svartholm, p. 367, Almqvist och Wiksell, Stockholm, 1968.

[16] D.J. Griffiths. *Introduction to Elementary Particles* , Wiley,(1987).

[17] C.-E. Wulz. *The CMS experiment at CERN.* , CMS CR 2005/026, 2005.

[18] The ATLAS Experiment, http://atlas.ch/index.html, last accessed date: 12 June 2008.

[19] W. M. Yao et al., *Particle Data Group* , J. Phys. G 33 (2006) 1.

[20] S.M. Bilenky, *The History of Neutrino Oscillations* , Phys. Scr. T121 17-22 ,(2005).

[21] Z. Maki, M. Nakagawa and S. Sakata, *Remarks on the unified model of elementary particles.* , Prog. Theor. Phys. 28, 870 (1962).

[22] V. N. Gribov and B. Pontecorvo,, *Neutrino astronomy and lepton charge* , Phys. Lett. B28, 493 (1969).

[23] L. Wolfenstein,D17, 2369 (1978); D20, 2634 ( 1979); S. P. Mikheyev and A. Yu. Smirnov, Yad. Fiz. 42, 1441 (1985) [Sov. J. Nucl. Phys. 42, 913 (1986)]; Nuovo Cimento 9C, 17 (1986).

[24] S. P. Mikheyev and A. Y. Smirnov, *Resonant amplification of neutrino oscillations in matter and solar neutrino spectroscopy* , Sov. J. Part. Nucl. 18, 188 (1987).

[25] Super-Kamiokande collaboration, Y. Fukuda et al., *Evidence for oscillation of atmospheric neutrinos*, Phys. Rev. Lett. 81, 1562 (1998), hep-ex/9807003.

[26] G. Barr, T. K. Gaisser and T. Stanev, *Flux of atmospheric neutrinos*, Phys. Rev. D39, 3532 (1989).

[27] D. Casper et al., *Measurement of atmospheric neutrino composition with IMB-3*, Phys. Rev. Lett. 66, 2561 (1991).

[28] W. W. M. Allison et al., *Measurement of the atmospheric neutrino flavour composition in Soudan-2*, Phys. Lett. B391, 491 (1997), hep-ex/9611007.

[29] M. C. Sanchez et al., *Observation of atmospheric neutrino oscillations in Soudan-2*, Phys. Rev. D68, 113004 (2003), hep-ex/0307069.

[30] J. N. Bahcall and R. K. Ulrich, *Solar models, neutrino experiments and helioseismology*, Rev. Mod. Phys. 60, 297 (1988).

[31] J. N. Bahcall and M. H. Pinsonneault, *Standard solar models, with and without helium diffusion and the solar neutrino problem*, Rev. Mod. Phys. 64, 885 (1992).

[32] J. N. Bahcall, M. H. Pinsonneault and S. Basu, *Solar models: Current epoch and time dependences, neutrinos, and helioseismological properties*, Astrophys. J. 555, 990 (2001), astro-ph/0010346.

[33] B. T. Cleveland et al., *Measurement of the solar electron neutrino flux with the Homestake chlorine detector*, Astrophys. J. 496, 505 (1998).

[34] GALLEX collaboration, P. Anselmann et al., *GALLEX results from the first 30 solar neutrino runs*, Phys. Lett. B327, 377 (1994).

[35] GALLEX collaboration, W. Hampel et al., *GALLEX solar neutrino observations: Results for GALLEX IV*, Phys. Lett. B447, 127 (1999).

[36] SAGE collaboration, J. N. Abdurashitov et al., *Measurement of the solar neutrino capture rate with gallium metal*, Phys. Rev. C60, 055801 (1999), astro-ph/9907113.

[37] SAGE collaboration, J. N. Abdurashitov et al., *Measurement of the solar neutrino capture rate by the Russian-American gallium solar neutrino experiment during one half of the 22-year cycle of solar activity*, J. Exp. Theor. Phys. 95, 181 (2002), astro-ph/0204245.

[38] Kamiokande-II collaboration, K. S. Hirata et al., *Real time, directional measurement of* $^8B$ *solar neutrinos in the Kamiokande-II detector*, Phys. Rev. D44, 2241 (1991).

[39] Super-Kamiokande collaboration, S. Fukuda et al., *Determination of solar neutrino oscillation parameters using 1496 days of Super-Kamiokande-I data*, Phys. Lett. B539, 179 (2002), hep-ex/0205075.

[40] Kamiokande-II collaboration, K. S. Hirata et al., *Results from one thousand days of real-time, directional solar-neutrino data*, Phys. Rev. Lett. 65, 1297 (1990).

[41] SNO collaboration, S. N. Ahmed et al., *Measurement of the total active* $^8B$ *solar neutrino flux at the Sudbury Neutrino Observatory with enhanced neutral current sensitivity*, Phys. Rev. Lett. 92, 181301 (2004), nucl-ex/0309004.

[42] CHOOZ collaboration, M. Apollonio et al., *Search for neutrino oscillations on a long base-line at the CHOOZ nuclear power station*, Eur. Phys. J. C27, 331 (2003), hep-ex/0301017.

[43] F. Boehm et al., *Final results from the Palo Verde neutrino oscillation experiment*, Phys. Rev. D64, 112001 (2001), hep-ex/0107009.

[44] KamLAND collaboration, T. Araki et al., *Measurement of neutrino oscillation with KamLAND: Evidence of spectral distortion*, Phys. Rev. Lett. 94, 081801 (2005), hep-ex/0406035.

[45] K2K collaboration, S. H. Ahn et al., *Indications of neutrino oscillation in a 250-km long- baseline experiment* ,Phys. Rev. Lett. 90, 041801 (2003).

[46] K2K collaboration, E. Aliu et al., *Evidence for muon neutrino oscillation in an accelerator-based experiment* ,Phys. Rev. Lett. 94, 081802 (2005).

[47] S. H. Ahn et al. [K2K Collaboration], Phys. Rev. D 74, 072003 (2006) [arXiv:hep-ex/0606032].

[48] MINOS collaboration, D. G. Michael et al., *Observation of muon neutrino disappearance with the MINOS detectors and the NuMI neutrino beam* ,Phys. Rev. Lett. 97, 191801 (2006).

[49] R.Acquafredda et al. (CNGS Coll.), *First events from the CNGS neutrino beam detected in the OPERA experiment*, New Journal of Physicsc, 8 (2006) 303.

[50] CNGS Project,*On line at http://proj-cngs.web.cern.ch/proj-cngs/*, last accessed date: 22 June 2008.

[51] M.Dracos (on behalf of the OPERA collabration), *The OPERA Experiment*,Physics of Atomic Nuclei.Vol.67, No.6, 2004, pp.1092-1096.

[52] A. Anokhina ,et al. *Emulsion Sheet Doublets as Interface Trackers for the OPERA experiment*,Apr 2008. 20pp. e-Print: arXiv:0804.1985 [physics.ins-det].

[53] T.Adam,et al. *The OPERA Experiment Target Tracker*,Nuclear Instruments and Methods in Physics Research, A 577 (2007) 523-539.

[54] M. Ambrosio, et al. Trans. Nucl.Sci. NS-51 (2004) 975.

[55] T. Nakamura,et al. *The OPERA film: New nuclear emulsion for large-scale, high-precision experiments*, Nuclear Instruments and Methods in Physics Research Section A: Accelerators, Spectrometers, Detectors and Associated Equipment Volume 556, Issue 1, 1 January 2006, Pages 80-86.

[56] A. Anokhina, et al. (OPERA Coll.), *Study of the effects induced by lead on the emulsion films of the OPERA experiment.*, e-Print: arXiv:0805.0123 [physics.ins-det], May 2008. 19pp.

[57] A. Garfagnini, et al. *The OPERA Experiment Muon Spectrometers*,Nuclear Instruments and Methods in Physics Research, A 572 (2007) 177-180.

[58] Giovanni De Lellis, *The OPERA Experiment*, Nuclear Physics B (Proc.Sppl.), 155 (2006) 203-204.

[59] J.E. Campagne for the OPERA collaboration, *The OPERA Experiment: $\nu_\mu \rightarrow \nu_\tau$ and $\nu_\mu \rightarrow \nu_e$ physics program.*, Eur Phys J C 33 ,s01, s837-s839 (2004).

[60] Y. Hayatos talk in this proceeding.

[61] M.Apolloni, et al.(CHOOZ Collobration) ,Phys. Lett. B 466, 415 (1999).

[62] E. Gschwendtner, A.Pardons et al. *First Operational Experience with The CNGS Facility*, contribution to NuFact07, 6-11 Agust 2007, Okayama,Japan.

[63] C. Lattes, H. Muirhead, G. Occhialini, C. Powell, *Process involving charged mesons*, Nature 159 (1947) 694-697.

[64] N. DAmbrosio, *A new automatic microscope for nuclear emulsion analysis*, Nuclear Instruments and Methods in Physics Research A 525 (2004) 193198.

[65] S. Aoki, et al., Nucl. Instr. and Meth. B 51 (1990) 466.

[66] T. Nakano, Ph. D. Thesis, University of Nagoya, 1997.

[67] C. Bozzas presentation, *Status and evolution of the European Scanning System*, in January 2008 in Nogoya.

[68] V. Tioukov, et al. *Framework for emulsion data reconstruction and analysis in the OPERA experiment.*, Nuclear Instruments and Methods in Physics Research A 559 (2006) 103105

[69] K. Hagiwara et.all., Physical Review D66, 010001-1 (2002).

[70] Particle Data Group., J.Phys. G: Nucl. Part. Phys. 33 (2006).

[71] M.J.Berger and S.M.Seltzer, *Tables of Energy Losses and Ranges of Electrons and Positrons.*, National Aeronautics and Space Administration Report NASA-SP-3012 (Washington DC 1964).

[72] E. Longo and I.Sestili, Nucl. Instrum. Methods 128, 283 (1975).

[73] W.R Nelson, T.M Jenkins,R.C McCall, and J.K. Kobb, Phys. Rev. 149, 201 (1966)

[74] W. Heitler, *The Quantum Theory of Radiation.*, 3rd ed., Oxford: Clarendon Press, 1953.

[75] R. Fernow, *Introduction to experimental particle physics.*, 1st ed., Cambridge University Press, 1986.

[76] M.Guler, et al.(OPERA Coll.), *Experimental Proposal*, CERN-SPSC-2000-28.